Pattern formation in two-frequency forced parametric waves

H. Arbell and J. Fineberg
The Racah Institute of Physics, The Hebrew University of Jerusalem, Jerusalem 91904, Israel
(Received 24 July 2001; published 5 March 2002)

We present an experimental investigation of superlattice patterns generated on the surface of a fluid via parametric forcing with two commensurate frequencies. The spatiotemporal behavior of four qualitatively different types of superlattice patterns is described in detail. These states are generated via a number of different three-wave resonant interactions. They occur either as symmetry-breaking bifurcations of hexagonal patterns composed of a single unstable mode or via nonlinear interactions between the two primary unstable modes generated by the two forcing frequencies. A coherent picture of these states together with the phase space in which they appear is presented. In addition, we describe a number of new superlattice states generated by four-wave interactions that arise when symmetry constraints rule out three-wave resonances.

DOI: 10.1103/PhysRevE.65.036224 PACS number(s): 89.75.Kd, 47.54.+r, 47.35.+i, 47.20.Gv

I. BACKGROUND

Patterns are ubiquitous in the world around us. The word ''pattern'' describes an order, regularity, or a simple mathematical description, which can be found either in a natural or a manmade system. Patterns often result from self-interactions of driven nonlinear systems. Naturally, the first patterns to be scientifically analyzed were the simplest ones, which can be described by few mathematical variables. However, in recent years we have learned to recognize and categorize patterns in systems that were assumed to be formless, devoid of any order. Perhaps the most obvious characteristics of these systems are the multiple length and time scales that can be present simultaneously. One of the most important mechanisms to explain such phenomena is the nonlinear resonant interaction between the different modes that are excited in these systems. In these interactions two or more waves can interact to form ''new'' waves. These waves have a wavelength and frequency that is the sum or difference of the basic waves. The system's energy can then be transferred between these modes or dissipated at different scales. The purpose of the work described in this paper was to explore this paradigm in the experimental study of a simple controlled system: the parametric excitation of waves on the surface of a fluid (the Faraday system).

The general form of the external acceleration applied to the system is given by

$$g(t)=A[\cos(\chi)\cos(m\omega_0 t)+\sin(\chi)\cos(n\omega_0 t+\phi)]. \quad (1)$$

This spatially uniform vertical excitation preserves the system's spatial symmetries while modifying its temporal ones.

As first noted by Faraday, sinusoidal acceleration (in the direction of gravity) of a fluid layer with angular frequency ω induces a pattern, having a wave number $k(\omega)$, on the fluid surface. Whereas waves excited by a single frequency have been studied extensively over the last 4 decades, the response of the system for multifrequency excitations has only recently begun to be investigated. Single-frequency driving can produce patterns of different symmetries. Patterns consisting of rolls, squares, hexagons, and 8-, 10-, and 12-fold quasipatterns have been experimentally observed in [1–4]. The secondary instabilities of these different patterns involve complicated states that display either spatiotemporal chaos [3,5–9], transverse amplitude modulations [10], or various defects [3,10] that break the patterns' initial global symmetry. The use of multiple-frequency driving enables us to study the interactions of different excited modes in a controlled way, as each excitation frequency can linearly excite a well-defined wave number. In this way, we hope to be able to slowly unfold the system's underlying behavior and thereby unravel the fundamental mechanisms that describe the waves' interactions.

The purpose of this paper is to provide a coherent overview of the wide variety of nonlinear states that result from two-frequency forcing. We will provide detailed descriptions of the spatial and temporal behavior of these states. In doing so, we will provide a characterization of these nonlinear states—depicting both the resonant mechanisms and symmetry constraints giving rise to their formation.

This paper is organized in the following fashion. In Sec. I we will briefly describe the theoretical and experimental work that has, to date, been performed in this system. The experimental apparatus and measurement techniques used in our measurements will then be described in Sec. II. We will then present, in Sec. III, an overview of the phase diagram together with a brief description of the different types of superlattice states observed. Each type of superlattice, together with the mechanisms that form it, will then be described in detail in the subsequent sections. A codimension-2 point, at χ_c, exists in this system where both externally driven modes simultaneously become linearly unstable. Subharmonic superlattice states (SSS), which bifurcate from an initial hexagonal state far from χ_c, will be described in Sec. IV. We will then progress to the region of phase space in the vicinity of χ_c. Three different types of superlattice patterns will be described in Secs. V, VI, and VII. All of the above superlattice patterns result from different types of three-wave resonant interactions. We will conclude with Sec. VIII in which a number of superlattice states generated by four-wave resonant interactions are described. We will show that these states can occur when three-wave interactions are forbidden.

A. Notation

The notation conventions used throughout this paper are as follows. The driving function is specified in Eq. (1). To

avoid confusion, we will always specify the driving frequency ratio used in Eq. (1) by the ratio m/n where m and n are the two co-prime integers that describe the two frequencies $\omega_1 = m\omega_0$ and $\omega_2 = n\omega_0$. We will always assume that $n > m$. In our notation, k_1 and k_2 refer to the wave numbers excited, respectively, by the driving frequencies ω_1 and ω_2. The angle χ in Eq. (1) describes the relative mixing between the two modes and the angle ϕ describes their phase difference, where the relevant range is $0 < \phi < 2\pi m/n$. $\cos(\chi)$ and $\sin(\chi)$ are sometimes [11,12] replaced by the mixing coefficients r and $1-r$.

In the following sections we will frequently characterize eigenmodes by their temporal parity. Since the parity of m and n is important we will use the notation odd/even (even/odd) to described the classes of driving where m (n) is odd and n (m) is even. Odd/odd describes driving where both m and n are odd. A state whose temporal response has a fundamental frequency of $\omega_0/2$ will be denoted as a ''subharmonic'' state, whereas a ''harmonic'' state is one with a fundamental frequency of ω_0.

We shall use the following units. The total amplitude A, appearing in Eq. (1), is measured in units of $g = 981\ \mathrm{cm}^2/\mathrm{sec}$. The fluid's kinematic viscosity ν is measured in centistokes ($0.01\ \mathrm{cm}^2/\mathrm{sec}$), and the depth of the fluid layer h is measured in centimeters. In many cases, we will identify, for simplicity, angular frequencies (e.g., ω) with the corresponding temporal ones [e.g., $\omega/(2\pi)$]. Where necessary, angular or temporal frequencies will be explicitly denoted. Unless otherwise noted, the spatial scales of the photographed states presented in the figures are $9 \times 9\ \mathrm{cm}^2$. Additional notation will be defined as needed.

B. Linear analysis

The linear stability analysis of the problem was performed by Besson, Edwards, and Tuckerman [13] by numerically solving the linearized Navier-Stokes equation via an extension of the technique developed by Kumar and Tuckerman [14] for single-frequency excitations. As in the single-frequency case, the acceleration–wave number plane is characterized by alternating tongues corresponding to the acceleration at which a given wave number becomes linearly unstable. For mixing angles $\chi = 0°$ and $\chi = 90°$ the tongue structure of single-frequency forcing with either $m\omega_0$ or $n\omega_0$ driving is obtained. Increasing χ from 0 results in the appearance of additional tongues whose dominant frequencies are spaced $\omega_0/2$ apart, since the system's basic frequency is then ω_0. Each odd-numbered tongue possesses a *subharmonic* temporal dependence composed of only frequencies $\omega_0(p + \frac{1}{2})$ whereas even-numbered tongues are temporally *harmonic*, i.e., composed of frequencies $p\omega_0$ (where p is any whole number). Although the time dependence of each tongue is given by an infinite series, the *dominant* frequency of the pth odd (even) tongue corresponds to $(p+\frac{1}{2})\omega_0$ ($p\omega_0$). Generally, within the critical tongues the dominant frequencies $n\omega_0/2$ or $m\omega_0/2$ have an order of magnitude greater amplitude than the other components. Thus, the temporal response of the critical modes for $m/n =$ odd/odd driving ratios is always subharmonic. For odd/even (even/odd), the k_1 ''tongue'' has a subharmonic (harmonic) response while the k_2 tongue has the opposite parity.

The system's critical wave number k_c corresponds to the lowest acceleration a_c at which the flat, featureless state loses stability. At a critical value of $\chi = \chi_c$, a codimension-2 point exists where two tongues having wave numbers k_1 and k_2 corresponding, respectively, to $m\omega_0/2$ and $n\omega_0/2$ simultaneously become unstable. For χ far from χ_c the critical wave numbers are close to the values of k_c obtained for single-frequency experiments. Near the codimension-2 point k_c tends to differ from the corresponding single-frequency value by up to 10%. The calculated values of both a_c and k_c are in excellent agreement with experiments [13,15]. While modes other than the critical ones are linearly damped, we will see that they can play an important role in nonlinear wave interactions.

C. Experiments with two-frequency forcing

In the case of single-frequency driving, the subharmonic time dependence prohibits quadratic terms in the ''amplitude'' equations describing the nonlinear interactions between the amplitudes of the excited modes. However, when using two-frequency driving with odd/even or even/odd parity, both harmonic and subharmonic temporal responses are possible. When one of the driving frequency components is dominant, one can consider the smaller component as a perturbation that breaks the system's temporal subharmonic symmetry. The reflection invariance of the corresponding set of coupled amplitude equations is then broken and, generically, quadratic terms can appear. These quadratic terms are important since they enable three-wave interactions between different modes.

Edwards and Fauve were the first to study the two-frequency driven Faraday instability [16–18]. They chose to focus most of their study on 4:5 driving although they also explored other ratios (such as $\frac{6}{7}$, $\frac{4}{7}$, $\frac{8}{9}$, and $\frac{3}{5}$). These experiments used a relatively viscous fluid and a small fluid layer height in order to minimize lateral boundary effects. As the viscosity of the fluid was rather high ($\nu = 100$ cS) stripe patterns occurred for single-frequency driving. The phase space as presented in [16] for (even/odd) 4:5 driving can be divided into two parts: The harmonic (subharmonic) part where the k_1 (k_2) wave vector is dominant and the leading temporal term has the frequency of $4\omega_0/2$ ($5\omega_0/2$). In the harmonic region, in place of the stripe patterns of wave number k_1 appearing for pure $4\omega_0$ driving, a first-order transition to hexagons occurs for $\chi > 10°$. In the subharmonic region, striped patterns with wave number k_2 are observed until the near vicinity of the codimension-2 point at χ_c. The first-order transition to the hexagonal state results from the quadratic interactions mentioned above.

In the neighborhood of the codimension-2 point, a temporally harmonic, 12-fold symmetric quasiperiodic pattern was observed. These states appeared for only a small range of ϕ ($\phi \sim 75° \pm 5°$). They evolved, via a first-order bifurcation, from either the flat zero-amplitude state or the subharmonic striped patterns. In the hysteretic region of these states, Edwards and Fauve also observed solitary axial waves that

originated from the quasiperiodic pattern. Arbell and Fineberg [19] have shown that these highly localized waves are related to ''oscillons,'' which are temporally oscillating states, observed in vibrating granular systems [20], that are highly localized in space.

Muller [12] later conducted two-frequency-forcing experiments using a driving ratio of $\frac{1}{2}$. These experiments were performed near χ_c in shallow fluid layers in various regions of the χ-ϕ phase space. Both temporally subharmonic hexagon and triangle patterns were observed. Triangular patterns are formed when the spatial phase associated with each of the excited eigenmodes differs from 0° or 180°. Muller showed that amplitude equations with both cubic and quintic terms (applying to temporally subharmonic waves) can form triangular patterns. In contrast, amplitude equations with quadratic terms have only stable hexagonal solutions. These experiments were later modeled by Zhang and Vinals [11] using a quasipotential approach. Experimentally, Muller showed that the addition of a third small-amplitude forcing frequency (which is equivalent to perturbatively breaking the system's parity) could stabilize either the hexagonal or triangular states.

More recent experimental studies in two-frequency-forced systems were performed by two groups, Kudrolli, Pier, and Gollub [21] and Arbell and Fineberg [15,19,22]. These studies were conducted both in the near vicinity and far from χ_c. They revealed a number of qualitatively new, superlattice-type states in which new scales, not directly introduced via the external forcing, were evident.

In regions of phase space that can be relatively far from χ_c, superlattice states were observed as secondary bifurcations from the harmonic $(m\omega_0/2)$ hexagonal states that occur for odd/even or even/odd driving ratios. The primary hexagonal symmetry with wave number k_c is broken by additional modes with wave numbers $q<k_c$ whose temporal response possesses an $m\omega_0/4$ component. These states include ''SL-II'' states observed for 4:5 driving by Kudrolli, Pier, and Gollub [21] and the (SSS) states observed for a large number of driving ratios by Arbell and Fineberg [15].

A second type of superlattice state is observed in the near vicinity of the codimension-2 point, once again on the side dominated by the *harmonic* driving component when even/odd or odd/even forcing is used. Two variants of these states coined ''SL-I'' [21] and double hexagonal states (DHS) [19] have been observed. These states can be described by the superposition of two hexagonal sets of wave vectors of magnitude k_c. The two sets of six wave vectors are oriented at an angle $\theta_r \simeq 22°$ to each other. This specific angle is not arbitrarily chosen. The sum and difference vectors between the two wave vector sets produce a sublattice spanned by the smaller difference wave vectors. When the two sets of wave vectors are oriented at specific angles of θ_r, the sublattice formed by the difference vectors becomes commensurate with the two hexagonal lattices. This structure is one of the generic possibilities that were anticipated on the basis of symmetry arguments proposed by Silber and Proctor [23].

A qualitatively different type of superlattice occurs in the vicinity of χ_c for all driving ratio parities. These states, coined two-mode superlattices (2MS) [15], are the most general of the superlattice states observed. They are formed by an interaction of the two linearly excited modes (k_1 and k_2) with a third linearly damped slaved mode that is nonlinearly excited. The angle between k_1 and k_2 is chosen by the following resonance mechanism: the vector difference $\vec{k}_2-\vec{k}_1$ produces a third wave vector $\vec{k}_3$. The magnitude of $\vec{k}_3$ is determined by the dispersion relation $\omega(k)$ for the difference frequency $\omega_3=\omega_2-\omega_1$.

An additional type of superlattice state has been observed for $\frac{2}{3}$ and $\frac{4}{5}$ driving in the vicinity of χ_c [22]. This state, which appears in place of the 2MS state, consists of a rhomboid pattern that is formed by the simple nonlinear resonance: $\vec{k}_2-\vec{k}_2'=\vec{k}_1$, where $|\vec{k}_2|=|\vec{k}_2'|$. When the coupling angle $\theta[\theta\equiv\cos^{-1}(\vec{k}_2\cdot\vec{k}_2'/k_2^2)]$ between $\vec{k}_2$ and $\vec{k}_2'$ is tuned to a value of $\theta\sim 2\pi/n$, $(2-n)$-fold quasicrystalline patterns are naturally formed.

D. Model equations and nonlinear analysis

Generally, two methods have been used to study the Faraday instability with two-frequency driving. The first uses simple model systems that yield qualitative insights regarding the behavior of the Faraday system. These use general assumptions based mainly on symmetry considerations. The second method is to start from the full nonlinear set of equations that describe the system, employ carefully chosen approximations, and derive a set of equations that describes the behavior of the system based on the real physical parameters. Both methods have yielded valuable insights.

1. Model equations

The observation of quasicrystalline patterns (''quasipatterns'') generated using two-frequency driving by Edwards and Fauve [16] and via single-frequency driving by Binks, Westra, and van de Water [24] provided a motivation to find model equations that display similar behavior. Muller [25] first considered a system of N coupled Landau equations with cubic nonlinear terms. These equations could be written as the gradient of a Lyaponov functional. Muller showed, by minimization of this functional, that regular N-fold patterns of different symmetries can be stable. Pattern selection depended on the value of the nonlinear coefficients coupling the linearly degenerate modes. This mechanism may be related to both the appearance of quasipatterns in single-frequency Faraday experiments and to the quasipatterns observed in the harmonic region of two-frequency Faraday systems with even/odd driving.

A second mechanism that can create quasipatterns is related to quadratic interactions between degenerate nonlinear modes. Muller proposed that a quadratic nonlinearity, generating the triad interaction $\vec{k}_2-\vec{k}_2'=\vec{k}_1$ ($|\vec{k}_2|=|\vec{k}_2'|$) could also lead to quasicrystalline patterns. The angle between $\vec{k}_2$ and $\vec{k}_2'$ is tunable by the ratio k_1/k_{2r} with resonant angles $\theta=45°$, 36°, and 30° for 8-, 10-, and 12-fold quasipatterns, respectively. These states were observed in a system of two coupled Swift-Hohenberg equations, each with a different unstable wave number. Frisch and Sonnino [26] also observed subcritical tenfold symmetrical patterns in coupled

Swift-Hohenberg equations. This state was numerically shown to be stable even when the dynamics are not derived from a free energy functional. In addition to states with *N*-fold symmetry, nonsymmetric, rhomboidal patterns were also seen to be stable for some parameter values. Later, both the rhomboidal patterns and resonant quasipatterns resulting from the above interactions were observed experimentally by Arbell and Fineberg [22].

Lifshitz and Petrich [27] modeled the two-frequency Faraday system with a single generalized Swift-Hohenberg-type equation for a *single* real field $u(x,y)$. This model is simpler than the coupled equations used by Muller, Frisch and Sonino, and Newell and Pomeau [28]. The model equation used was rotationally invariant with *two* built-in critical wave numbers. The equation contained a quadratic term that both broke the system's up-down symmetry and allowed triad wave interactions. Stable striped, hexagonal and 12-fold symmetric patterns were observed for different values of the control parameter. In addition to these *N*-fold symmetric states, a compressed hexagon state, similar to the rhombic/stripe pattern described by Muller, was observed.

The above model systems suggest that the existence of two unstable wave numbers together with the possibility of triad interactions (provided by quadratic terms) is a sufficient condition for the formation of quasiperiodic patterns. Another common feature of these models is the existence of distinct regions of phase space in which patterns that lack *N*-fold symmetry are stable.

2. Nonlinear analysis

In contrast to the simplified model systems described above, Zhang and Vinals [11] derived a description of the system's dynamics from the governing equations for the two-frequency Faraday problem. To this end, they applied the quasipotential approach developed for single-frequency study [29] to the problem of two-frequency driving. This approach is strictly valid in the limits of weak dissipation and infinite fluid depth.

To compare their results with Muller's experimental results, Zhang and Vinals analyzed the special case of $\frac{1}{2}$ driving in depth. They first used the linearized equation to study the location of the codimension-2 point, χ_c, as a function of the phase difference ϕ. The results were in qualitative agreement with the experiments. The discrepancies were attributed to the high damping used in Muller's experiment, which was outside the region of validity of the theory. It is interesting to note that the dependence of χ_c on ϕ is a special feature of $\frac{1}{2}$ driving and does not occur for other driving combinations.

Zhang and Vinals then, using a multiple scales approach, derived standing wave amplitude equations. This weakly nonlinear analysis assumed that the system was far from the codimension-2 point, so that a single temporal mode dominated the dynamics. For the case of $\frac{1}{2}$ driving, they first obtained a prediction for the relative magnitudes of the different Fourier components of the weakly nonlinear temporal response of the fluid surface. Then, assuming *N* degenerate modes, the coupled amplitude equations describing these modes were derived. In contrast to [25], the function $\beta(\theta_{ij})$ coupling the ith and jth modes was computed from the physical parameters of the problem. One interesting result of this calculation was that the phase difference ϕ can have a strong effect on the coupling function β and thereby a strong effect on the nonlinear pattern selection. The relative stability of different *N*-fold nonlinear states was then calculated by minimization of a Lyapunov functional, as in [25,27]. Semiquantitative agreement with the regions of stability observed experimentally in [12] for different patterns (squares, hexagons/triangles, and quasipatterns of various orders) observed in the subharmonic region of the ϕ-χ phase space was obtained.

An important result of this work was that it suggested a new type of physical mechanism that governs the selection process. These calculations indicated that the value of the coupling coefficients was strongly influenced by triad interactions between the linearly excited modes (corresponding to the dominant excitation frequency) and the *linearly stable* modes corresponding to the *second* excitation frequency. Resonant coupling to these latter modes served, in the region of phase space far from χ_c, to enhance the effective damping—as energy transferred to these ''slaved'' modes is more efficiently dissipated. Far from χ_c, states that *cannot* couple to the slaved modes are then preferred by the system. As we shall later see, however, in the *vicinity* of χ_c, resonant triad coupling to the linearly stable, slaved modes provides one of the main mechanisms for the rich variety of nonlinear states observed.

Silber and Skeldon [30] were the first to theoretically study the two-frequency Faraday system in the vicinity of the codimension-2 point. This study pointed out the importance of accounting for the temporal symmetries of the system. Silber and Skeldon focused on forcing ratios m/n having either odd/even or even/odd parities, where interactions between harmonic and subharmonic waves may occur.

As shown in [11], resonant mode interactions greatly affect the mode coupling function $\beta(\theta)$. Using normal form analysis, Silber and Skeldon showed that triad resonances $\vec{k}_1 \pm \vec{k}_1' = \vec{k}_2$ (where $k_1 = k_1'$) are only possible when the temporal mode corresponding to k_2 is harmonic. When k_2 has a subharmonic temporal dependence, quadratic terms in normal form equations can be eliminated [31,32]—thereby decoupling the harmonic modes from the subharmonic ones. This can be simply understood since the product of two linear eigenfunctions (resulting from a quadratic interaction term) results in the addition of their temporal phases. The sum of *two* harmonic or subharmonic temporal phases cannot produce a subharmonic one, therefore two modes of like parity cannot couple quadratically to a subharmonic state. Silber and Skeldon [30] went on to demonstrate the above, by calculating the amplitude equations for both $\frac{1}{2}$ (odd/even) or $\frac{2}{3}$ (even/odd) driving by means of the quasipotential approximation used in [11].

The existence or suppression of three wave resonances can have a significant effect on the qualitative features of the phase diagram. When one is far from χ_c we have seen [11] that three-wave resonant coupling influences pattern selection by enhancing dissipation via the coupling to a heavily damped (slaved) mode. In this case, resonant triads are strongly *suppressed*. On the other hand, when in the near

vicinity of χ_c, resonant coupling to nearly unstable linear modes can occur. Moreover, if these modes undergo a first-order bifurcation, their growth will be (to first order) unchecked and resonant coupling to them may have a very significant effect on the spatiotemporal behavior of the system.

Silber, Topaz, and Skeldon [33] have recently demonstrated the importance of resonant coupling to slaved modes for $\frac{6}{7}$ forcing near χ_c. Using the quasipotential approximation [11] they showed how weakly damped linear modes with wave numbers $K<k_c$ quadratically couple to the unstable modes to create the SL-I states observed by Kudrolli, Pier, and Gollub [21]. In this case, the critical wave vectors $|\vec{k}_i|=k_c$ could be constructed from a commensurate hexagonal sublattice of wave vectors $\vec{K}_i$ such that $\vec{k}_i=q\vec{K}_1+p\vec{K}_2$. The SL-I states are a particular case where $(p,q)=(\pm 2, \pm 3)$ with $k_c/K=\sqrt{7}$. This particular coupling was made possible by the existence of a weakly damped linear tongue with a wave number close to K. The SL-I state was *not* observed for $\frac{2}{3}$ forcing since, for this forcing ratio, no linear tongues near this resonance exist since there are no additional harmonic modes with $K<k_c$ (K_i must be harmonic by [30] as they result from the vector difference of two $\vec{k}_i$ modes).

Recent work by Tse, Rucklidge, Hoyle, and Silber [34] has shown that the SL-II states observed by Kudrolli, Pier, and Gollub [21] may be understood as resulting from a symmetry-breaking bifurcation of an initial hexagonal symmetry. Study of the possible invariant subgroups of the original D_6+Z^2 symmetry characterizing hexagonal standing waves revealed a number of possible solution branches. One of these corresponds to the spatial symmetry of temporally averaged SL-II-type states. Depending on the normal form coefficients, five additional possible solution branches were predicted. It remains to be seen whether these other branches are experimentally observed.

II. EXPERIMENTAL SYSTEM

Our experimental system consisted of a shallow fluid layer, laterally bounded by a plastic sidewall and mounted on a computer-controlled mechanical shaker. A 1-cm-thick, black-anodized aluminum plate of 14.4 cm diameter supported the fluid from below. This plate was machined to a 10 μm flatness. The mechanical shaker used (either Unholtz-Dickie model 5PM or VTS model 100) provided vertical accelerations ranging from 0 to 15g. The cell acceleration, regulated to within 0.01g, was monitored continuously by a calibrated accelerometer (Silicon Designs, INC 1210L-010) attached directly to the armature of the shaker. A feedback mechanism was used to control and stabilize the amplitude A, mixing angle χ, and phase ϕ to desired values.

Most of our experiments were conducted with Dow Corning 200 silicone oil of different viscosities (DC200/10, DC200/20, DC200/50, and DC200/100). Silicone oil has a typical density of 0.95 g/cm^3 and surface tension of 21.5 dyne/cm. This fluid is Newtonian for the viscosity range of 1–100 cS. Since the fluid viscosity is highly temperature dependent, stabilizing the fluid temperature was important. A stable fluid temperature of $30\pm 0.05\,^{\circ}$C was used in all experiments. Resultant viscosity variations were less than 0.04 cS. A number of experiments were also performed using TKO-77 vacuum pump fluid with viscosities ranging between 221 cS at 33° and 184 cS at 30°. Both Dow Corning 200 and TKO-77 have very low vapor pressures so there was no need to seal the cell against evaporation. The results of our experiments showed no dependence on the particular type of fluid used.

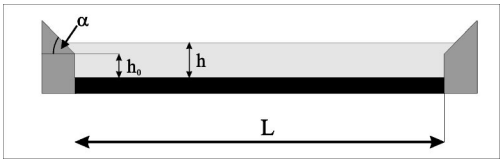

FIG. 1. A profile of the container used is shown: a Delrin circular boundary (gray) is attached to the bottom plate (black). The boundary consists of a vertical section of height h_0 and an inclined section at an angle of $\alpha=20°$ chosen to allow the surface of the liquid used, Dow Corning 200, to be at zero contact angle with the rim (liquid in light gray). Rings with h_0 of 1, 1.5, 2.5, 4, and 5 mm were used. h could be changed continuously by adding small amounts of fluid with a calibrated pipette.

Our experiments were performed at frequencies between 20–150 Hz. The selection of the frequency was influenced by the aspect ratio of the patterns and the shaker's maximum acceleration and stroke. Frequency selection was also influenced, to a lesser extent, by limitations of the imaging and laser probe technique. Typically the aspect ratio between the cell diameter L and the wavelength λ was between $5<L/\lambda<50$. The maximal driving frequency of 150 Hz was governed by a_c, which increases with increasing ω. The shaker's maximal stroke (2.5 cm, peak to peak) and boundary mode quantization at small aspect ratios dictated the lower frequency limit.

A. Boundary conditions

The lateral boundary conditions of the experimental cell can have an important effect on the waves excited by the system. In our experiments we attempted to minimize the role of the sidewalls. A circular shape for the lateral boundary was chosen. This ensured that no particular pattern was preferred. This is especially significant when the system is only slightly dissipative (e.g., low viscosity fluids and/or large fluid depth). For a more highly dissipative system (e.g., high viscosity fluids and/or shallow fluids), the boundary's shape does not influence the symmetry of the excited pattern [18].

As discussed by Douady [1], an additional effect of sidewalls is the possible emission of waves (meniscus waves) from the lateral boundaries. These waves are forced at the driving frequency via forced height variations of the meniscus formed at the contact line between the fluid and lateral boundaries. Meniscus waves have no threshold and can therefore mask the instability threshold of parametrically forced waves. To minimize this effect, our system's lateral boundaries (shown schematically in Fig. 1) were sloped at an

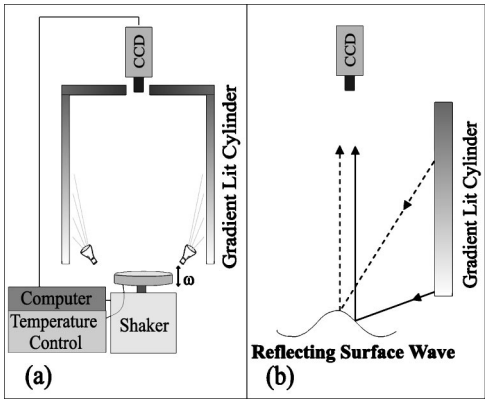

FIG. 2. (a) A schematic diagram of the experimental system. The imaging system consisted of a cylindrical screen, concentric with the experimental cell, which was illuminated by halogen lamps arranged in a circle. A CCD camera was mounted on the cylinder axis above the fluid surface. (b) The cylinder's illumination intensity was varied as a function of the height above the fluid. At each point on the fluid surface the local slope reflects only a single point from the cylinder surface into the CCD. Since the lighting provides a unique intensity at each height along the cylinder, the intensity reflected by each point is uniquely mapped to the projection of the fluid surface's slope in the direction of the cylinder axis.

angle conjugate to the contact angle between the fluid and the material (Delrin) from which the lateral rings were constructed. (A slope of $\alpha = 20°$ was used for the Dow Corning 200 silicone oil.) In this way, we ensured that the static fluid interface was nearly flat.

An additional advantage of sloped lateral boundaries is the elimination of reflected waves by impedance matching. Since the instability threshold increases with decreasing h, a gradual decrease (sloping sides) in fluid depth increases the effective local threshold at the larger radii to far beyond a_c. Since the typical height of the fluid layer in the sloped region was only 0.1–0.8 mm, parametric waves could not be excited and any meniscus waves emanating from the wall were strongly damped. In practice, this boundary condition combined with the fluid viscosities and depths used enabled us to obtain values of a_c within 2% of the calculated values [13,35,36] for a system of infinite lateral extent.

B. Visualization

1. Imaging from above

To visualize the fluid surface, we employed an alternative type of imaging technique. The imaging system is schematically shown in Fig. 2(b). The experimental cell was illuminated by a tall cylindrical screen whose axis was concentric with center of the cell. The screen was illuminated from below by a ring of 12 small lamps. As a result, the light intensity along the screen varied as a function of the height above the fluid. A charge-coupled device (CCD) camera was mounted on the cylinder axis, 1.4 m above the cell. At each point on the fluid surface [see Fig. 2(b)], the local slope reflects only a single point from the screen onto the CCD. Since the lighting provides a unique intensity at each height along the cylinder, the intensity reflected by each point on the fluid surface is uniquely mapped to the projection of its slope on the cylinder axis. We used the CCD's high-speed shuttering mode (1/1000 sec) to obtain instantaneous images of the fluid surface.

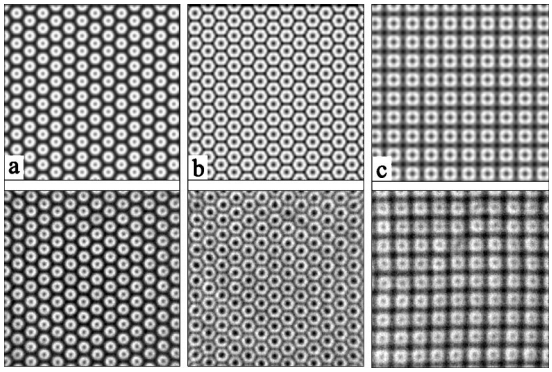

FIG. 3. Using the method described in the text we calculated model images (top) of a simple hexagonal state in its peak state (a) and crater state (b) and of a square state (c). The corresponding experimental patterns are shown (bottom). To model the surface waves we assumed an asymmetry between up hexagons and down hexagons due to the the fact that the hexagon's amplitude was large compared to the small layer height.

Two methods of triggering were used to control the CCD camera. The first method employed a trigger signal that was synchronized with the driving. This signal both reset the camera and initiated acquisition of the video frame at a desired phase relative to the driving signal. To observe slow changes in the patterns over long times, slow trigger rates that were commensurate with the driving frequency were used. The short-term behavior of a state in its different temporal phases was studied by the use of slightly incommensurate trigger rates. This allowed nearly continuous acquisition of the different temporal phases of a given state without the need for very high-speed acquisition.

Our imaging technique, although providing quantitative information, does not directly yield the surface wave height function $h(x,y)$. The imaging yields a gray-scale image, $I(x,y)$, that is approximately the absolute value of the gradient of the height function, i.e.,

$$I(x,y) = \sqrt{[\partial_x h(x,y)]^2 + [\partial_y h(x,y)]^2}. \tag{2}$$

One must then work backwards from $I(x,y)$ to determine the function $h(x,y)$. This is done by inputting an assumed state into Eq. (2) and comparing the computed pattern to the state observed. By iteration it is possible to arrive at fairly good estimates of $h(x,y)$. Some examples are presented in Fig. 3.

For high-amplitude states, visualization from the side was sometimes used. This was performed by illuminating from the side and placing a video camera in the horizontal plane of the plate at the height of the system's lateral boundary. This configuration enabled direct quantitative measurements of the wave amplitudes adjacent to the lateral boundaries of the cell. An additional advantage of this imaging was that it allowed us to simultaneously view both the lower plate's vertical movement together with the wave's motion. In this way their relative phase could be directly measured.

C. High resolution temporal measurements

Most previous studies of the Faraday system have used imaging techniques that mainly yield information about the symmetries of the states observed. Time domain information was generally extracted by the use of stroboscopic lighting at the frequency of the shaker. This technique measures the lowest frequency in which a state oscillates but yields no information about higher harmonics. Two experimental studies used a laser beam probe to extract information about the surface waves. Douady [1] used a laser beam deflected at an angle from the surface waves and reflected on a screen to study the amplitude of the waves. Simonelli and Gollub [37] used a laser beam deflected from the surface waves onto a photodetector to obtain temporal information. This technique, however, could not give precise information about the slope of the fluid surface since an average intensity reflected from a single ''cell'' of the pattern was measured.

We combined these two methods by imaging the reflection at the fluid surface of a highly focused laser onto a position sensitive detector (UDT SL20). This method yielded an accuracy of 1–5 % in the surface slope and a temporal resolution of 0.02 mS. A good signal-to-noise ratio was obtained by amplitude modulating the laser signal and then deconvolving the resultant signal of the position sensitive detector (PSD). The temporal response of the system was only limited by the maximal sampling frequency of the PSD voltage.

III. OVERVIEW OF THE PHASE DIAGRAM

The phase space of the two-frequency Faraday system is very large. Besides physical parameters such as fluid layer height and viscosity, one also has to set the driving parameters. Introducing two driving components with different frequencies, different amplitudes and a nontrivial relative phase makes the task of choosing a working regime and the relevant dimensionless combinations of parameters a difficult one.

We have chosen to focus on the simplest commensurate driving ratios as a first step. The m/n ratio combinations used in our experiments were numerous: $\frac{1}{2}$, $\frac{2}{3}$, $\frac{2}{3}$, $\frac{2}{5}$, $\frac{2}{7}$, $\frac{3}{4}$, $\frac{3}{5}$, $\frac{3}{7}$, $\frac{4}{5}$, $\frac{4}{7}$, $\frac{5}{6}$, $\frac{5}{7}$, $\frac{5}{8}$, $\frac{6}{7}$, $\frac{6}{11}$, $\frac{41}{60}$, $\frac{40}{59}$, $\frac{21}{50}$. Most of our detailed experiments were performed with no phase difference between the two frequency components [$\phi=0$ in Eq. (1)]. For system parameters that were seen to excite special patterns, scans of ϕ were made. Changing ϕ was found to be crucial for the existence of some of the states and of no relevance to others. Phase diagrams were constructed by fixing the mixing angle χ and increasing the amplitude A until a state of droplet ejection was reached.

Two typical two-frequency phase diagrams for even/odd driving are presented in Fig. 4. In single-frequency experiments rolls, squares, hexagons, and quasipatterns of different symmetries are known to exist depending on the viscosity, height, frequency, and amplitude above the threshold. In our parameter regime, the dominant structure in regimes dominated by a single frequency is squares for low viscosities ($\nu=8.7-23$ cS) and both squares and rolls for higher viscosities ($\nu=47-87$ cS). As in other studies of two-frequency driving [12,16,17], two main regions, dominated by either k_1 or k_2, exist. Each of these regions has not only a different wavelength but also different temporal behavior. The k_1 and k_2 dominated regions have a strong response at $\omega_1/2$ and $\omega_2/2$, respectively. This is true for all values of m/n. The temporal response, however, consists of additional frequency components that depend on the ratio m/n. When both m and n are odd (odd/odd driving) the excited surface modes in both regions of phase space have only subharmonic components [i.e., $(p+\frac{1}{2})\omega_0$ with p an integer]. In the case of odd/even (even/odd) driving, the k_1 dominated region is temporally subharmonic (harmonic) while the k_2 dominated regime is temporally harmonic (subharmonic). At the critical value $\chi=\chi_c$, a codimension-2 point exists where both wave numbers are simultaneously linearly unstable. The k_1 dominated region occurs for $\chi<\chi_c$ while the k_2 dominated region occurs for $\chi>\chi_c$. The interaction of k_1 and k_2 leads to a variety of different nonlinear states in the vicinity of χ_c. Before describing these states, we will first describe the effects of two-frequency driving in the two main regions *far* from χ_c.

In the regions dominated by harmonic states we have found a number of nontrivial states that bifurcate from single-mode hexagonal states while breaking both their spatial and temporal symmetries. These symmetry-breaking bifurcations can even occur when χ is quite small. The SSS [Fig. 4 (bottom)] is an example of such a symmetry-breaking state. SSS states are formed in the k_1 dominated regime with $\chi_c-5°\geqslant\chi\geqslant 10°$, when the primary hexagonal state's symmetry with harmonic temporal behavior is broken by an additional set of wave vectors of magnitude $q<k_1$ with subharmonic temporal behavior (frequency $\omega_1/4$) with respect to the primary $\omega_1/2$ frequency. We have observed two main types of SSS states, which differ from each other in the orientation, magnitude, and number of $\vec{q}$ wave vectors. For example, the SSS state shown in Fig. 4, (SSS type I) breaks the initial hexagonal symmetry by the introduction of two wave vectors $\vec{q}$, which are parallel to two of the three initial wave vectors $\vec{k}_1$. The magnitude of q in this case is $k_1/2$, which yields a simple resonance condition $\vec{q}+\vec{q}=\vec{k}_1$. SSS have been observed only for even/odd driving for *all* of the m/n combinations listed above. The different SSS types and the mechanisms that form them will be described in detail in Sec. IV.

For even/odd driving, the effect of two-frequency driving on the pattern formation in the k_2 dominated region is quite different than in the k_1 dominated region. In the k_2 region, square symmetry dominates at threshold from $\chi=90°$ to $\chi\approx\chi_c$. Only in the vicinity of χ_c do we see the effects of the two-frequency driving on the patterns formed. It is interesting to note that although theory predicts that hexagons are preferred for harmonic response and squares for subharmonic response (see Sec. I), we have observed *square* symmetry in large parts of the harmonic region for odd/even driving ($\chi>\chi_c$).

Let us now briefly describe the patterns formed for even/odd driving in the vicinity of χ_c. Starting with the k_1 dominated ($\chi<\chi_c$) region, two types of patterns are observed

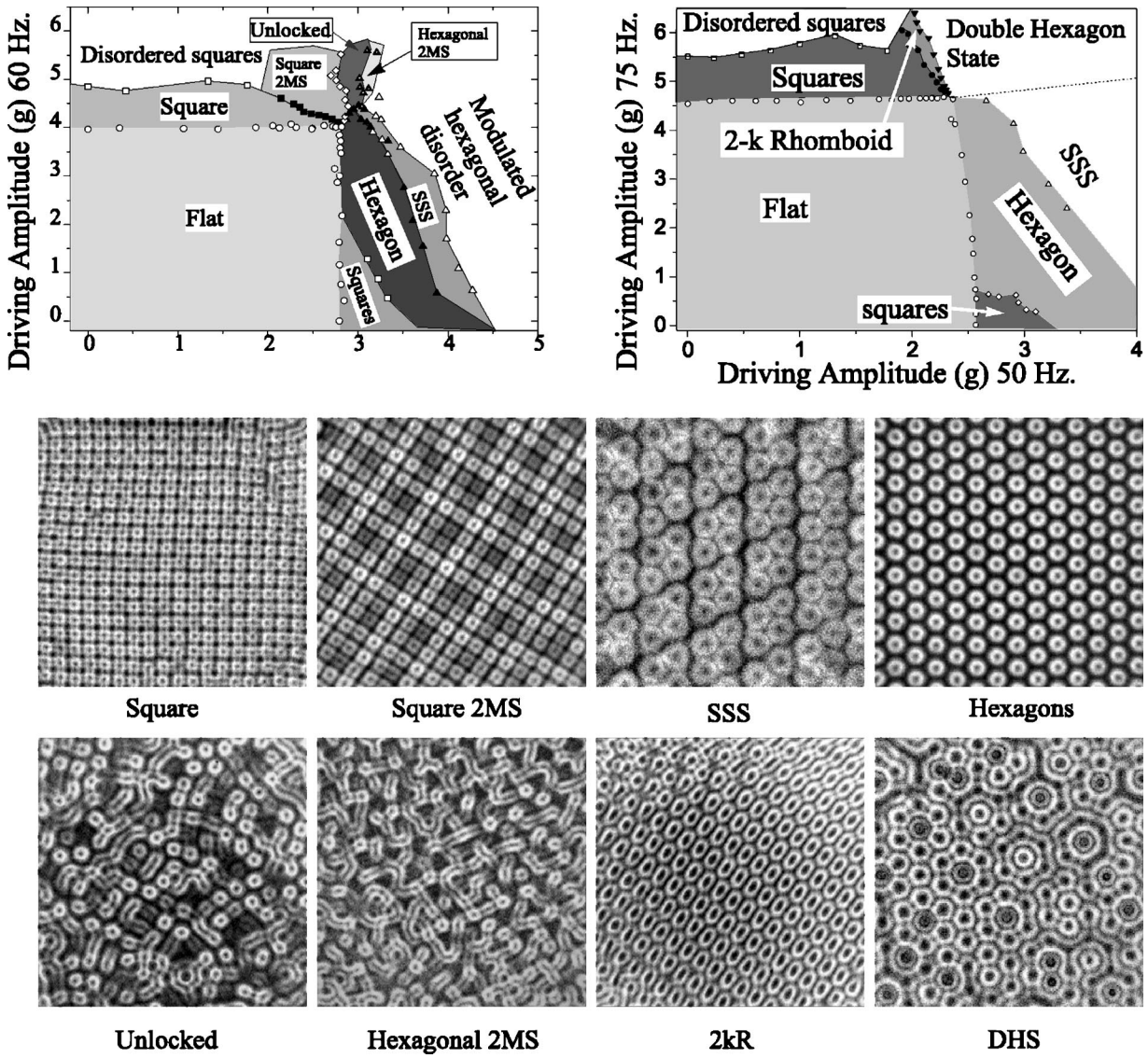

FIG. 4. Two typical phase diagrams of two-frequency experiments obtained for 2:3 driving with different system parameters: $\omega_0 = 20$ Hz and $h = 0.155$ cm (left) and $\omega_0 = 25$ Hz and $h = 0.2$ cm (right). In both experiments $\nu = 23$ cS and $\phi = 0°$. Square regions exist in the near vicinity of single-frequency forcing. The square symmetry dominates in the subharmonic regime to near χ_c while throughout most of the harmonic region the hexagonal symmetry dominates. In the vicinity of the codimension-2 point we observe three new states that exist for many combinations of the driving ratio. These states are two-mode superlattices (2MS), with underlying square or hexagonal symmetries and spatially and temporally unlocked states (''Unlocked'' states). A resonant state that consists of a rhomboid unit cell ($2kR$) was also observed (right). Unlike the 2MS and unlocked states, which appear for many different driving ratios (odd/odd, odd/even, and even/odd), this state was observed for only for $\frac{2}{3}$ and $\frac{4}{5}$ driving. In the harmonic region of phase space where hexagons are initially dominant, a second bifurcation occurs to either temporally subharmonic states (subharmonic superlattice state, SSS) or high-amplitude waves (as well as, at times, localized ''oscillon'' waves) that appear on a double hexagonal superlattice (DHS). Symbols in the phase diagram describe measured transitions for fixed χ. Bottom: typical photographs of these states.

near χ_c. One pattern, which we call the double hexagonal state (DHS) is formed by two sets of hexagonally arranged wave vectors (of length k_1) with a finite angle α between them. In the phase space shown in Fig. 4, $\alpha \sim 22°$. In contrast to the SSS, this state does *not* break the temporal symmetry of the harmonic hexagon state. Depending on various system parameters, DHS's are sometimes formed by a first-order bifurcation. Perhaps their most outstanding characteristic is their very high amplitude. The surface wave maxima can reach amplitudes much higher than the fluid layer's height. In [19] we have shown how the DHS's can form oscillons, a highly localized large-amplitude nonlinear state that has been observed [19,20,38] in a number of periodically driven systems.

A special case of the DHS occurs for $\alpha = 30°$, whence one obtains 12-fold quasipatterns such as first observed in [16]. We have seen the formation of such patterns for $\frac{4}{5}$ driving in the same region where the DHS with $\alpha = 22°$ appears for $\frac{2}{3}$ driving.

Let us now move to the vicinity of χ_c both on the border

of the k_1 region and within the k_2 region. Here two linearly unstable eigenvectors with different magnitudes can be concurrently excited. There are numerous possible configurations in which such a system can organize itself. Four different classes of mixed mode states were found to exist. These will be described in detail in Sec. VI.

Two-mode superlattices. These states are formed by the interaction of the dominant mode (e.g., k_2), with its original symmetry, and the weaker mode (e.g., k_1), which breaks the symmetry of the original pattern. The symmetry of the dominant mode can be either square or hexagonal depending on the proximity of the nearest primary state in phase space. In Fig. 4 we present two types of 2MS modes, a square 2MS obtained for $\chi > \chi_c$ and a hexagonal 2MS obtained for $\chi < \chi_c$. The temporal behavior of the 2MS contains both the $\omega_1/2$ and $\omega_2/2$ frequency responses and always includes the subharmonic frequency of $\omega_0/2$. These states appear for all types of driving (odd/even, even/odd, and odd/odd) although the precise structure of phase space depends on the driving ratio used.

Unlocked states. Between the square and hexagonal 2MS states an intermediate region exists where both k_1 and k_2 appear but no well-defined symmetry or spatial mode locking is observed. Thus, no long-range correlations in either space or time exist. The basic time scale of the surface waves is $T=4\pi/\omega_0$ but the pattern changes its local structure over time scales of order 10^2-10^3T.

Rhomboidal states. Changing h, ν, or ω_0 can lead to qualitative changes in the phase space. Figure 4 shows two different phase diagrams obtained for $\frac{2}{3}$ driving. The only difference between the two diagrams is the fluid layer height and the value of basic frequency ω_0. Lioubashevski, Arbell, and Fineberg [39] describe how the dimensionless number δ/h, defined by the ratio between the effective boundary layer depth $\delta=\sqrt{\nu/\omega_0}$ and the fluid height h, affects single-mode states selected by the system. For a certain range of δ/h, rhomboidal patterns replace the 2MS and unlocked states (see Fig. 4, bottom). These states couple two wave vectors of length k_2 with one wave vector of length k_1. These wave vectors evolve *spontaneously* from two circles of linearly degenerate states. We will show that for special parameter values, n-fold quasipatterns can naturally evolve from the rhomboidal structures.

In addition to the states described above, in Sec. VIII we will show examples of a number of other resonant structures that are formed for different system parameters. The richness of this system allows one to observe a wide variety of different resonant patterns. We will show some common traits of these resonant selection mechanisms that can lead to a more comprehensive understanding of resonant interactions in pattern forming systems.

IV. SUBHARMONIC SUPERLATTICE STATES

Hexagonal patterns can be formed in two-frequency experiments when the basic subharmonic temporal invariance is broken and quadratic nonlinear terms appear in the amplitude equations describing the system. These terms can occur in regions of the two-frequency phase space that have a harmonic response. By increasing the amplitude of the driving, the primary hexagonal symmetry can be broken and new *stable* structures appear even in regions where the second externally driven mode cannot be excited at all. In this section we will describe the characteristics of these symmetry-breaking patterns.

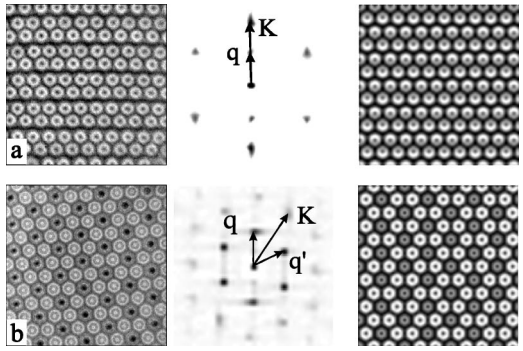

FIG. 5. For $\frac{2}{3}$ driving we observe two types of temporally subharmonic superlattices, the SSS-I (a) and SSS-II (b). Experimental images (left) together with their spatial power spectra (middle) and simulated images (right) are shown. In (a) we see that a small vector of magnitude $q=K/2$ ($\vec{q}\|\vec{K}$) breaks the hexagonal symmetry formed by primary wave numbers $\vec{K}_i$, where $K_i=k_c$. In (b) the primary hexagonal symmetry is broken by wave vectors $q=K/\sqrt{3}$ located at a 30° angle relative to the primary wave vectors. Both patterns can exist in regions far from χ_c, where the higher odd-frequency component is weak (see Fig. 4). The patterns obey the resonance conditions $2\vec{q}=\vec{k}_c$ (SSS-I) and $\vec{q}+\vec{q}'=\vec{K}$ (SSS-II).

In the notation used in this section, $\vec{K}$ is the linearly unstable wave vector, excited $\omega_1=m\omega_0$, that characterizes the primary pattern. $\vec{q}$ is an additional smaller wave vector that appears in states that bifurcate from the primary pattern. Since in each pattern there is a degeneracy in the direction of the wave vectors, we will use an index to number the different wave vectors of the same magnitude, e.g., $\vec{K}_i$, $i=1,2,\ldots$.

Subharmonic superlattice states occur over a wide range of χ in the two-frequency phase diagram where the lower frequency ω_1 is dominant. SSS were observed for most even/odd frequency ratios tested, but were *not* seen for odd/even or odd/odd ratios. Since the first SSS-type state was found [15], additional variants have been observed for different experimental parameters. Both types of SSS pattern, SSS-I [Fig. 5(a)] and SSS-II [Fig. 5(b)] are shown with their corresponding spatial power spectra. Both states share the following characteristics: The basic temporal dependence of both SSS types is subharmonic with respect to the the primary instability, i.e., the system has a strong response at $m\omega_0/4$; these states are secondary bifurcations of temporally harmonic hexagonal states; both states occur in the same basic region of phase space (for $0<\chi<\chi_c$); In both states k_2 wave vectors are *not* observed.

The different states, in general, occur for different fluid parameters such as fluid viscosity, fluid depth, and ω_1/ω_2 ratios. The most obvious differences can be seen in Fig. 5. Examining their spatial power spectra, we see that while both SSS-I and SSS-II spectra are constructed by three

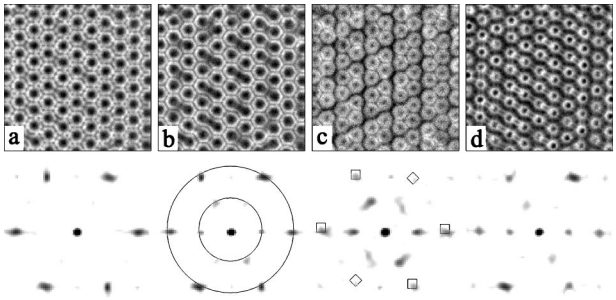

FIG. 6. Typical temporal sequences of an SSS-I state (a) taken at constant values of the driving parameters for the frequency ratio $\frac{40}{60}$ Hz. The spatial Fourier spectra are composed solely of wave numbers K, corresponding to $\omega_1/2$, and $q=K/2$. The *locations* of the peaks are fixed in the different temporal phases. For the system parameters $\omega_0/(2\pi)=20$ Hz, $\nu=23$ cS, $\phi=0°$, and $h=0.155$ cm, the hexagonal symmetry is broken in *two* directions by the $K/2$ vectors. Circles of radii K and $K/2$ are drawn in (b). The relative intensities of the different wave vectors can be seen; in (a) $\vec{q}_i$ are nearly absent while in (c) their intensities are almost equal to the $\vec{K}_i$. The symmetry breaking is also revealed in the intensities of the primary hexagonal vectors, as can be seen in (c), where the two strong intensity wave vectors are enclosed in a square and the weak one in diamonds.

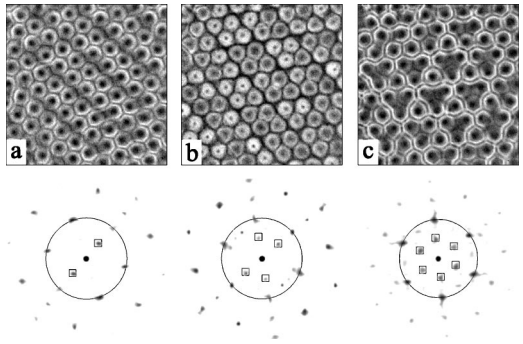

FIG. 7. Images (top) and power spectra (bottom) of an SSS-I type state with broken symmetry in one (a) two (b), and three (c) directions. The circles indicate the primary hexagon wave vector's magnitude, K. The symmetry-breaking vectors of magnitude $q=K/2$ are enclosed in squares. All images were obtained for the same system parameters of $\nu=23$ cS ($\frac{40}{70}$ Hz and $h=0.155$ cm, $\chi=43°$ and $\phi=0°$). This pattern is not stable and drifts slowly (order of 10–60 sec) between these three states.

evenly spaced wave vector pairs $\vec{K}_i$, the spectra include additional sets of wave vectors $\vec{q}_i$ (where $|q_i|<K$) of smaller magnitude. The orientations and magnitudes of $\vec{q}_i$ *differ* in SSS-I and SSS-II states.

In SSS-I $\vec{q}_i$ are oriented solely along (some or all of the) axes defined by the $\vec{K}_i$. The lengths of the q_i in the SSS-I are usually $K/2$, but in some cases the $q_i \neq K/2$.

SSS-II states are formed by a set of $\vec{q}_i$ that *always* consists of three evenly spaced wave vector pairs of magnitude $q=K/\sqrt{3}$ arranged at an angle of 30° relative to the direction of the $\vec{K}_i$ triad. The magnitude and orientation of q_i yield the simple resonance condition $\vec{q}_1+\vec{q}_2=\vec{K}_i$. While the SSS-I have been observed for a wide range of driving ratios ($\frac{2}{3}$, $\frac{4}{7}$, $\frac{2}{5}$, $\frac{2}{7}$, $\frac{4}{5}$), the SSS-II have only been seen for $\frac{2}{3}$ and $\frac{4}{5}$ driving. Both types of SSS states have recently been identified as representations of different invariant subgroups when hexagonal symmetry is broken [34,40].

In the following sections we will present a detailed description of each of the SSS types together with a mechanism that can explain their formation.

A. Subharmonic superlattice type I

The spatiotemporal behavior of the SSS-I state can be modeled by a simple equation for the surface height function,

$$h(r,t)=\cos(\tfrac{1}{2}m\omega_0 t)\sum_{i=1}^{3} A_i \cos(\vec{K}_i\cdot\vec{r}+\alpha_i) + \cos(\tfrac{1}{4}m\omega_0 t+\gamma)\sum_{i=1}^{M} B_i \cos(\vec{q}_i\cdot\vec{r}+\beta_i), \quad (3)$$

with

$$\vec{q}_i \| \vec{K}_i, \quad \beta_i = 0°, 90°, \quad (4)$$

where M is the number of axes with broken symmetry, γ is the *temporal* phase difference between the two sets of modes, and α_i and β_i are the respective *spatial* phases of the $\vec{K}_i$ and $\vec{q}_i$ components. Because the pattern has hexagonal symmetry we assume $\alpha_i=0°$ and not $\alpha_i=2\pi/3$ as in patterns having triangular symmetry [12]. Equation (3) summarizes the most important features of the SSS-I in a compact way. We will now present experimental evidence for the validity of this equation and describe the relevance of each term (A_i, B_i, γ, β_i, and M) in the experimentally observed states.

In Fig. 6 we present a sequence of SSS-I states taken at different times for constant values of the driving parameters. Although the states' appearance changes with time, their spatial Fourier spectra reveal that the state results from the interaction of two specific spatial scales; the primary wave number $|\vec{K}|=|\vec{k}_1|$ that is excited by the ω_1 frequency component and its spatial subharmonic, $\vec{q}=\vec{K}/2$. The SSS spectra show that while the $\vec{K}_i$ have six-fold symmetry, two $\vec{q}_i$ with relatively large amplitude and a third smaller amplitude $\vec{q}_i$ have broken this symmetry. The amplitudes of the q_i vary with time. Within the temporal phases shown in Fig. 6(a) the q_i amplitudes have little power while in Fig. 6(c) the $\vec{q}_i$ are stronger than the $\vec{K}_i$ components. This behavior is reflected by the temporal phase γ in Eq. (3). The symmetry breaking is reflected by the relative strengths of both the $\vec{q}_i$ and $\vec{K}_i$. It is clear that the two K wave vectors enclosed in squares have different strength than the wave vector enclosed in diamonds. This symmetry breaking is also seen in the relative power of the q_i wave vectors.

As demonstrated in Fig. 7, SSS states can have broken symmetry in one, two, or three directions [$M=1,2,3$ in Eq. (3)]. In most cases, a specific number of symmetry-breaking

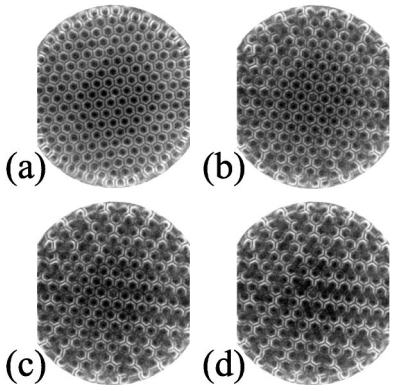

FIG. 8. The transition between hexagonal and the SSS state is displayed for a typical experiment (40/60). This is a gradual process in which the basic symmetry of a perfect hexagonal pattern (a) is broken first at the circular boundary (14.4 cm) of the cell. As the amplitude of the external forcing increases, the area of broken symmetry grows inwards (b),(c) until the SSS state fills the entire cell (d). This process can also occur in the reverse direction.

directions was selected. However, for the experiment described in Fig. 7, the pattern drifted slowly (on the scale of seconds) between the three possible symmetry-broken states.

The transition between the primary hexagonal pattern and the SSS states is (within $\approx 1\%$) *nonhysteretic* and occurs via a circular front that propagates slowly inward from the plate's lateral boundaries. The process is continuous and reversible (see Fig. 8). Before continuing the study of the spatial characteristics of the SSS-I pattern let us digress briefly and examine the temporal behavior of the system using the laser probe method (see Sec. II C).

Typical time series of the x and y components of the fluid surface gradient at a single point are presented in Fig. 9 for three different accelerations. These describe the temporal behavior of hexagons at threshold (a), developed hexagons (b), and SSS-I (c). At threshold, the response is harmonic with respect to the total period of $2\pi/\omega_0$. The response is strongest at the frequency of $\omega_1/2$. Increasing the driving amplitude results in a bifurcation to a state with a strong *superharmonic* response at the frequency of ω_1. This phenomenon also occurs for single-frequency experiments.

A further increase of the driving amplitude yields a second bifurcation. In this bifurcation the temporal response becomes *subharmonic* with respect to the period of $2\pi/\omega_0$. As can be seen in Fig. 9 the superharmonic component does not disappear and can be quite strong. It is important to note that $2/n$ driving has some special relations between the various frequencies that are not present for higher-order driving (such as $\frac{4}{5}$, $\frac{4}{7}, \ldots, \frac{6}{7}, \ldots$). For $2/n$ driving $\omega_1/2=\omega_0$. The temporal response in the harmonic region has the same frequency as the common frequency ω_0. In other driving ratios, such as $\frac{4}{5}$ driving, the subharmonic is $4\omega_0/2=2\omega_0$ where the common frequency is ω_0. It is possible that such a relation can enhance certain resonant mechanisms and help stabilize certain patterns such as the $2kR$ and oscillon states [19,22].

Wagner, Muller, and Knorr [41] studied a two-mode system generated by single-frequency excitation at a bicritical point where both harmonic and subharmonic tongues become unstable. They describe two different superlattice states that exist in the transition region between subharmonic squares to harmonic hexagonal states. In the first superlattice state, the square symmetry is broken by a small wave vector $\vec{k}_D$ that is equal to $\vec{k}_H$-$\vec{k}_S$, where $\vec{k}_H$, $\vec{k}_S$ are, respectively, the primary hexagonal and square wave vectors. The relative phase of the symmetry breaking k_D mode compared to the primary square k_S mode can either be 0° or 90° according to the sign of the nonlinear coefficient in the amplitude equation for the symmetry-breaking mode. The experimental observation shows that the phase selected for the first transition state is 90°. A second superlattice state [41] was observed that is similar to the SSS-II states found in our experiments. The spatial phase difference β between the harmonic hexagonal mode and the subharmonic symmetry-breaking mode was found to be 0° although from amplitude equation considerations 90° is also a possible solution.

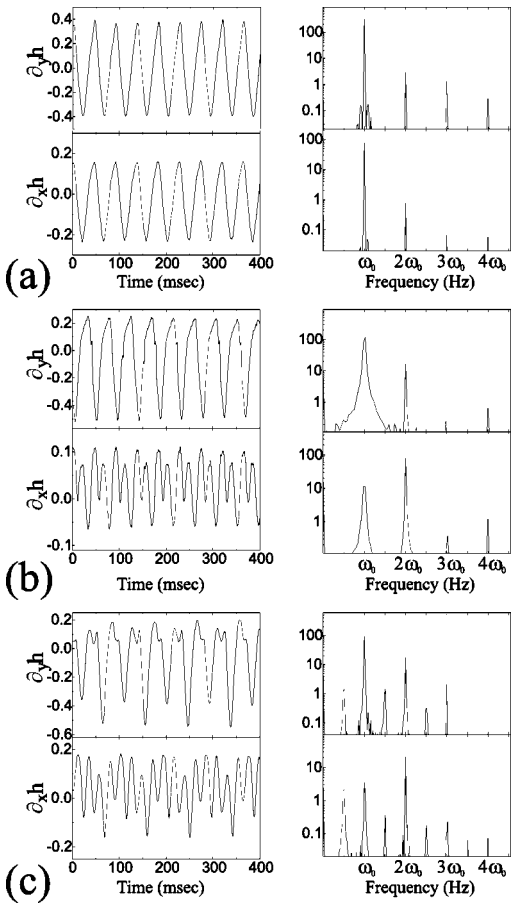

FIG. 9. The time dependence of the SSS-I state as studied by the reflection of a laser by the surface waves. In this experiment, for system parameters $\omega_0/(2\pi)=22$ Hz, $\nu=23$ cS, $h=0.2$ cm, $\phi=0°$, and $\chi=36.3°$, increasing the driving amplitude from 2.5 g (a) to 2.9 g (b) and 3.7 g (c) results in (a) low-amplitude hexagons, (b) developed hexagons, and (c) SSS-I states. In (a) both $\partial_x h$ and $\partial_y h$ have the same peaks in their power spectrum. Increased driving amplitude yields a different temporal response in the two directions x and y. This phenomenon also occurs in single-frequency experiments where squares are dominant and may be a general feature of the Faraday instability in viscous fluids. In the SSS-I state (c) a subharmonic temporal response at $\omega_0/2$ occurs.

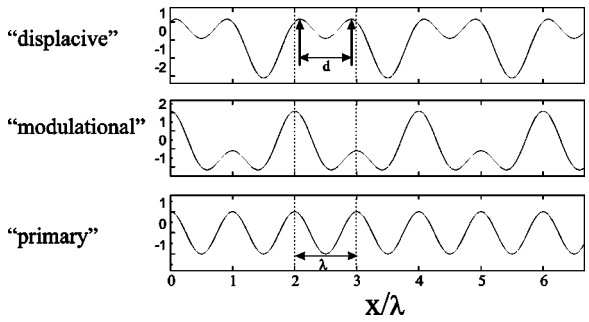

FIG. 10. A simple one-dimensional superposition of a harmonic function (bottom) $\cos(2\pi x/\lambda)$ with its subharmonic can have two basic combinations. The ''displacive'' mode shown results from the superposition of $\cos(2\pi x/\lambda)+b\cos(\pi x/\lambda+\pi/2)$ (top) ($b=2.2$ is arbitrarily chosen), whereas a ''modulational'' mode results from the superposition of $\cos(2\pi x/\lambda)+b\cos(\pi x/\lambda)$ (middle). It can be seen that in the ''displacive'' mode the distance between local maxima is either d or $2\lambda-d$ with $\lambda-d\ll\lambda$, while in the ''modulational'' mode the distance between the local maxima remains the same as in the primary mode, λ.

We will now describe in detail the effects of this phase difference on SSS-I states with broken symmetry. Let us first consider the effect of adding a $K/2$ modulation in one dimension. In Fig. 10 we can see that adding the $K/2$ mode with $\beta_i=0°$ results in a modulation of the original cosine form. The waves' local maxima remain at the same spatial location but their amplitudes are now modulated with a $4\pi/K$ periodicity resulting in one large peak followed by a smaller peak. In contrast to this, adding the $K/2$ mode with $\beta_i=90°$ results in a different effect. While all of the maxima have the *same* amplitude, their spatial *locations* are modulated with a $4\pi/K$ periodicity. This effect [41] is called ''displacive.'' The spatial effect in images can be quite pronounced. This is demonstrated in Fig. 11 where we present a comparison between the ''displacive'' (left) and ''modulational'' (right) effects with spatially subharmonic patterns and symmetry breaking along one direction (top) or three directions (bottom). The effects of symmetry breaking in three directions are more complicated but the qualitative effect remains. We find that SSS-I states are *always* of the displacive nature ($\beta=90°$). This can be seen by comparing the experimental images shown in Fig. 7 with the simulated displacive patterns shown in Fig. 11.

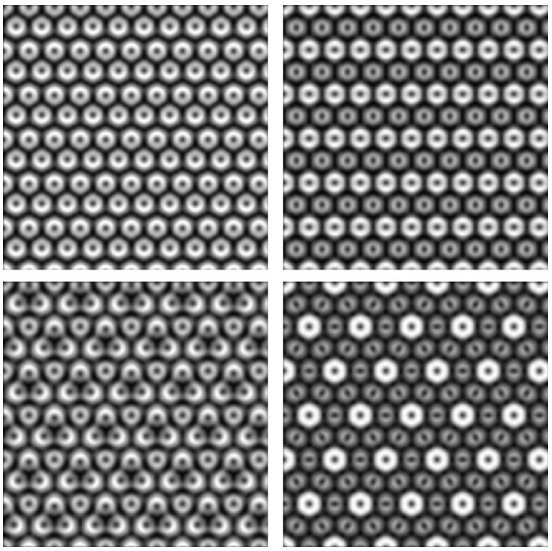

FIG. 11. ''Displacive'' (left) and ''modulational'' patterns (right) are shown for both symmetry breaking in one (top) and three directions (bottom). The pattern shown is simulated using our imaging model applied to Eq. (3) with $M=1$ ($M=3$) for one direction (three directions) and with $\beta_i=\pi/2$ ($\beta_i=0$) for the ''displacive'' (''modulational'') patterns. 2:3 forcing was used with amplitudes of all modes taken to be equal ($A_i=B_i$). All SSS-I patterns were found to be displacive in character (compare to Fig. 7).

It is interesting to note that the ''modulational'' pattern shown in Fig. 11 (bottom right) was seen in an experimental study of the single-frequency Faraday system in a viscoelastic fluid [42]. When changing the driving frequency, Wagner, Muller, and Knorr found both a harmonic region for low driving frequencies and a subharmonic response for higher ones. In the vicinity of the transition frequency, Wagner observed a hexagonal superlattice composed of both the subharmonic and harmonic wave vectors. Since the subharmonic wave vector is exactly half of the harmonic one, the simple resonance of $\vec{k}_S+\vec{k}_S=\vec{k}_H$ is retained (where the S index stands for subharmonic and the H for harmonic). Although the power spectra of this superhexagon described by Wagner, Muller, and Knorr are similar to the SSS-I power spectra (in the case of three-direction symmetry breaking), the real space patterns are different, indicating a 0° spatial phase difference between k_S and k_H, in contrast to the $\beta_i=90°$ seen for SSS-I.

The combination of the spatial displacive mechanism and the subharmonic temporal dependence of the $K/2$ mode results in an interesting ''jittering'' effect in time. If we consider Eq. (3) we see that when $t\rightarrow t+2\pi/\omega_0$ the first term in the right-hand side of Eq. (3) is invariant whereas the second term changes sign due to the different time dependence. In our model calculation the temporal displacement of $2\pi/\omega_0$ is equivalent to a spatial displacement of $2\pi/K$ in each of the symmetry-breaking directions. Images photographed at time intervals of $2\pi/\omega_0$ appear to jitter at this scale.

B. Subharmonic superlattice type II

As mentioned above, a qualitatively different type of SSS-type pattern, SSS-II, has been observed. Increasing both viscosity and height but keeping the dimensionless parameter δ/h constant (by changing ω_0) results in a different symmetry-breaking scenario. Though the SSS-II appears in the same region of phase space as the SSS-I and shares its subharmonic temporal behavior, it is qualitatively different from the SSS-I. The excited vectors $\vec{q}_i$ are now aligned at an angle of $\pi/6$ relative to the vectors $\vec{K}_i$ (in contrast to $\vec{q}_i\|\vec{K}_i$ in type SSS-I). The symmetry-breaking wave vectors are of magnitude $|q_i|=|K_i|/\sqrt{3}$ and these states exhibit *no* spatial symmetry breaking. For each $\vec{K}_i$ there is a corresponding $\vec{q}_i$.

Our experiments suggest that SSS-II can be described by

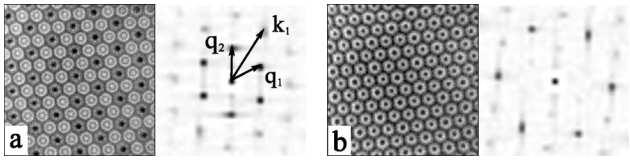

FIG. 12. Images [(a),(b) left] with corresponding power spectra [(a),(b) right] of different temporal phases of an SSS-II state observed for $\frac{2}{3}$ driving in the harmonic region of phase space at $\nu = 47$ cS [$\omega_0/(2\pi) = 25$ Hz and $h = 0.2$ cm]. In contrast to the SSS-I pattern, where the primary hexagonal symmetry is broken by wave vectors parallel to $\vec{K}_i$, SSS-II feature a different symmetry breaking. A second hexagonal lattice of smaller magnitude wave vectors forms, obeying the resonance condition $\vec{q}_1 + \vec{q}_2 = \vec{K}$. At certain temporal phases the effect can be easily seen (a) while at others only the hexagonal symmetry is dominant (b).

$$h(r,t) = \cos(\tfrac{1}{2} m\omega_0 t) \sum_{i=1}^{3} A_i \cos(\vec{K}_i \cdot \vec{r} + \alpha_i) + \cos(\tfrac{1}{4} m\omega_0 t) \sum_{i=1}^{3} B_i \cos(\vec{q}_i \cdot \vec{r} + \beta_i), \qquad (5)$$

$$\vec{K}_1 = K(0,-1), \quad \vec{K}_2 = K\left(\frac{\sqrt{3}}{2}, \frac{-1}{2}\right), \quad \vec{K}_3 = K\left(\frac{-\sqrt{3}}{2}, \frac{-1}{2}\right),$$

and

$$\vec{q}_1 = q(-1,0), \quad \vec{q}_2 = q\left(\frac{1}{2}, \frac{\sqrt{3}}{2}\right), \quad \vec{q}_3 = q\left(\frac{1}{2}, \frac{-\sqrt{3}}{2}\right),$$

$$q = \frac{K}{\sqrt{3}}.$$

Looking at this state at different temporal phases, the effect of the q_i can be easily seen at some phases [Fig. 12(a)] while, at others, only the hexagonal symmetry is apparent [Fig. 12(c)]. This symmetry is a representation of one possible invariant subgroup when hexagonal symmetries are broken [34,40,43].

In the $\frac{1}{2}$ driving experiments performed by Muller [12] a transition between hexagonal and triangle patterns was observed that corresponds to a change of $\Sigma_i \alpha_i$ in Eq. (5) from the value of 0 to $3\pi/2$ [where the second term of the rhs of Eq. (5) is zero]. A similar phenomenon can take place with SSS-II states. As shown in Fig. 13, a variant of the SSS-II states occurs with a rotational symmetry of $2\pi/3$ in contrast to the $2\pi/6$ that is typical for hexagon patterns. These SSS-II variants are observed for $\frac{2}{3}$ driving when relatively higher frequencies ($\omega_0 > 40$ Hz) are used. Using our imaging model, we find that these patterns are formed by the same resonance as the SSS-II but when spatial phase angles of the $\vec{q}_i$ modes are $\beta_i = \pi/2$ for $i = 1$, 2, 3 or $\Sigma_i \beta_i = 3\pi/2$. These SSS-II states have symmetries that are similar to those of the time-averaged symmetries and wave numbers of the ''SL2'' states observed in [21]. The instantaneous images of SL2 states, however, are more reminiscent of SSS-I states (as shown in Fig. 6). Patterns similar to this SSS-II variant have recently been observed in a forced ferrofluid system [44] in the vicinity of a bicritical point where harmonic and subharmonic solutions collide. Muller shows that when considering a harmonic region amplitude equation with quadratic terms for a single wave number model, only solutions where $\Sigma_i \beta_i = 0$ are possible. It appears that the second set of equations for the q wave number modes, which are temporally *subharmonic*, does allow the existence of modes with $\Sigma_i \beta_i = 3\pi/2$ solutions. The mechanism that selects the spatial phase in multimode systems still must be clarified.

SSS-II type patterns have also been observed in the experimental study of optical pattern formation in sodium vapor [45]. In the following section we will address the question of a selection criterion between the SSS-I and SSS-II states.

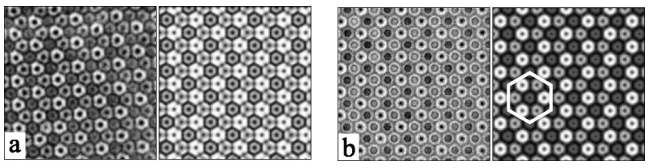

FIG. 13. For $\frac{2}{3}$ driving and $\nu = 0.47$ cS, a SSS-II type pattern with a different spatial dependence occurs. Two phases of this state are shown in [(a), (b) (left)] and a simulation of these patterns is shown in [(a), (b) right]. These patterns are formed when the spatial phases of the smaller wave vectors, $\vec{q}_i$, are shifted by $\pi/2$ relative to $\vec{K}_i$. These states were observed for higher frequencies ($\omega_0 > 35$ Hz) than those for which SSS-II having a zero phase shift are observed.

C. Selection between SSS-I and SSS-II

Both SSS-I and SSS-II break the temporal symmetry of the initial hexagon state by temporal period doubling to a basic frequency of $m\omega_0/4$. The two states, however, differ in their spatial behavior. For the case of SSS-I states, the excited wave vectors, $\vec{q}_i$, are both parallel to the linearly unstable wave vectors $\vec{K}_i$, and, in many cases $q = K/2$. In contrast, the excited wave vectors in SSS-II states are rotated by $\pi/6$ relative to $\vec{K}_i$. What mechanism governs the selection of both the two different states and the values of q that are excited?

As Silber, Topaz, and Skeldon have suggested [33], the symmetry-breaking wave vectors of harmonic patterns may correspond to minima of linearly stable tongues that can be excited via nonlinear coupling to the $\vec{K}_i$ modes. Since the subharmonic frequency $m\omega_0/4$ is excited by all of the SSS states, the linearly stable tongue with a dominant $m\omega_0/4$ frequency would be a likely candidate to be selected. The wave number q corresponding to these waves can be well approximated by the linear dispersion relation $q = k(m\omega_0/4)$. Note that q is not constant for a given value of ω_0, but can be strongly dependent on the parameters ν and h.

Let us now examine the following premise. The system will generically prefer to undergo spatial period doubling to $q = K/2$. If, however, $\vec{q}(m\omega_0/4)$ is close to a wave vector $\vec{q}$ with a magnitude that is substantially different than $K/2$, one possible solution of the system is to lock to either SSS-I or

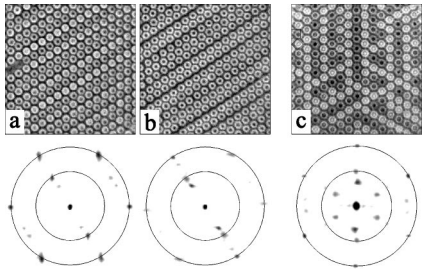

FIG. 14. Images (top) and corresponding power spectra (bottom) of SSS-I superlattices observed for $\frac{2}{3}$ driving in which $q \neq K/2$. Circles of a radii K (outer) and q, corresponding to the $m\omega_0/4$ frequency (inner) are drawn. The primary hexagonal symmetry is broken either in one direction (a), (b) or in three directions (c). (a), (b) show the same state at different temporal phases. The relative intensities of $\vec{q}$ and $\vec{K}-\vec{q}$ vary in the different phases. All experiments were with $\nu=23$ cS. (a), (b) for $h=0.2$ cm and (c) for $h=0.25$ cm. The basic frequency was $\omega_0/(2\pi)=35$ Hz for (a), (b) and $\omega_0/(2\pi)=30$ Hz for (c). The value of q/K is ≈ 0.6 for all experiments.

SSS-II patterns with $q \neq K/2$. If q is near $K/\sqrt{3}$, the system will lock to this value, thereby fulfilling the spatial resonance condition: $\vec{q}_i+\vec{q}_j=\vec{K}_i$. SSS-II patterns will then occur. Values of q sufficiently far from either spatial resonance will result in an SSS-I state with $q \neq K/2$. Such a state is presented in Fig. 14 where symmetry breaking occurs in either one direction [Figs. 14(a) and 14(b)] or three [Fig. 14(c)] but the symmetry-breaking wave vector's magnitude was *not* $K/2$. Instead, vectors parallel to $\vec{K}_i$, with magnitudes $q \neq K/2$ and $K-q$ are observed with, empirically, $q \sim 0.6k_c$.

This premise is checked in Fig. 15, where we plot the value of the ratio between the experimentally measured values of q and the wave number computed for single-frequency driving using $m\omega_0/4$ with K for parameters where different SSS-type patterns were observed. The plot shows that for both SSS-II and the SSS-I with $q \neq K/2$ the approximation $q=k(m\omega_0/4)$ is correct to within 4%. In SSS-I states where

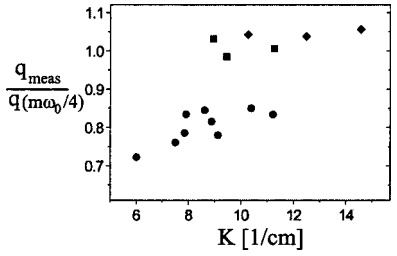

FIG. 15. The measured wave number q_{meas} of the symmetry-breaking wave vectors in SSS-type patterns, normalized by the linear wave number calculated for the frequency $m\omega_0/4$ as a function of the measured critical wave number of the primary hexagon pattern, K. The symbols correspond to different types of SSS patterns; SSS-I patterns with $q=K/2$ (circles), SSS-I with $q \neq K/2$ (diamonds), and SSS-II patterns with $q=K/\sqrt{3}$ (squares). The data indicate that the first type of pattern ($q=K/2$) is generally preferred by the system unless the value of $q(m\omega_0/4)$ is either close to $q=K/\sqrt{3}$ or sufficiently far from either of these preferred modes.

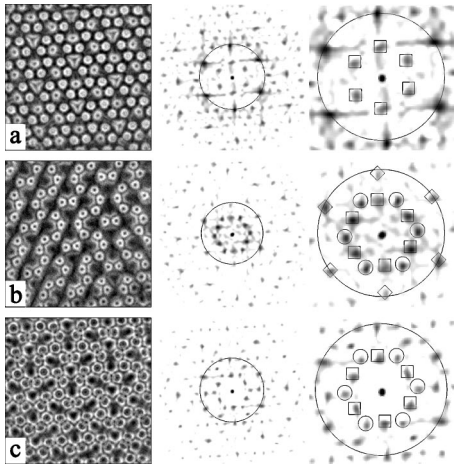

FIG. 16. Reducing h from $h=0.33$ cm, where only SSS-II was observed, to $h=0.31$ cm results in a state where the two types of SSS patterns SSS-I and SSS-II can coexist. In (a)–(c) the combined state images (left), full power spectra (middle), and expanded power spectra (right) are presented at different temporal phases. The primary hexagonal symmetry (of magnitude $\vec{k}_0$) is broken by two different sets of wave vectors arranged in two sixfold sublattices. The set corresponding to the SSS-I is enclosed in squares. The set corresponding to the SSS-II is enclosed in circles. This state was observed for $\frac{2}{3}$ driving and system parameters of $\nu=47$ cS, $\omega_0/(2\pi)=25$ Hz, $h=0.31$ cm, $\chi=62.5°$, and $\phi=0°$.

$q=K/2$ is the symmetry-breaking mode, the ratio $q/k(m\omega_0/4)$ varies *systematically* between 77%–85 %. This suggests that the $\vec{q}=\vec{K}/2$ resonance is strong enough to induce this "locking" or detuning of q.

For $\frac{2}{3}$ driving we observed the appearance of SSS-I states at lower liquid layer depth and the SSS-II at higher depths. As h is reduced, we found that instead of an abrupt transition between the SSS-I and SSS-II states, both types of symmetry breaking can occur *simultaneously*. As shown in Fig. 16, the primary hexagonal symmetry of this state is broken by two sixfold sets of wave vectors.

One set corresponds to SSS-I with magnitude $q_0=K/2$ while the other set corresponds to SSS-II, with $q_1=K/\sqrt{3}$. In real space the characteristic pattern of SSS-II [Fig. 16(b)] is broken by superimposed stripes in one direction. This state has both modulative and displacive effects implying that the two symmetry-breaking modes retain their respective spatial phase characteristics.

As demonstrated in Fig. 15, the mechanism that forms both the SSS-I and the SSS-II patterns depends on a "slaved" linear eigenmode. In the $\frac{2}{3}$ driving described above, the only existent linearly stable subharmonic tongue occurs for $\omega_0/2=m\omega_0/4$. In contrast to $\frac{2}{3}$ driving, even/odd driving ratios with m/n values such as $\frac{4}{5}$, $\frac{6}{7}$, etc., possess linearly stable tongues whose dominant frequencies differ from $m\omega_0/4$. For example, in $\frac{50}{75}$-Hz driving, besides the 15 Hz ($=m\omega_0/4$) response observed for the SSS state, a response at 7.5 Hz ($=\omega_0/2$) is also possible. Recent theoretical work by Silber, Topaz, and Skeldon [33] has suggested that these additional slaved modes can influence the character of the selected nonlinear state. We find that these additional slaved

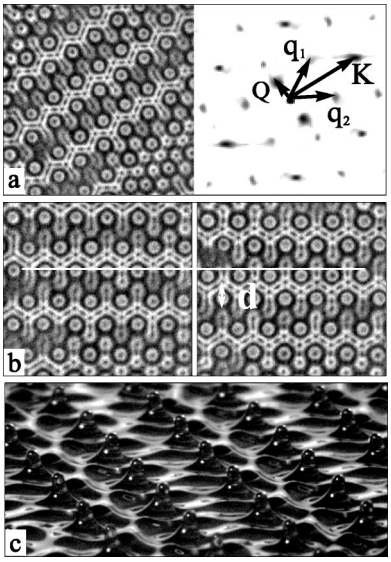

FIG. 17. (a) The image (left) and power spectrum (right) of ''cascaded'' SSS states appearing for $\frac{4}{5}$ driving near χ_c. The two mechanisms appearing in SSS-I and SSS-II coexist at different scales. A hexagonal sublattice of $q_i = K/\sqrt{3}$ bifurcates from the original hexagonal pattern. In addition, a *third* wave vector $\vec{Q} \neq \vec{q}$ breaks the symmetry of this sublattice in a single direction. This state has an overall temporal periodicity of $2\pi/\omega_0$. This is demonstrated in (b) where two images [(b) left, right] were taken at an interval of π/ω_0. The images are displaced by a $d = 4\pi/K$ length scale. The horizontal white line indicates the location of the peaks in the first phase [(b) left]. (c) A side view of this state. The peaks are of high amplitude and have the characteristic shape of the oscillons described by Arbell and Fineberg [19] with a small asymmetry in the direction of $\vec{Q}$. These images were observed for system parameters of 75/60 Hz, $\nu = 23$ cS, $h = 0.2$ cm, $\chi = 56°$, and $\phi = 0°$.

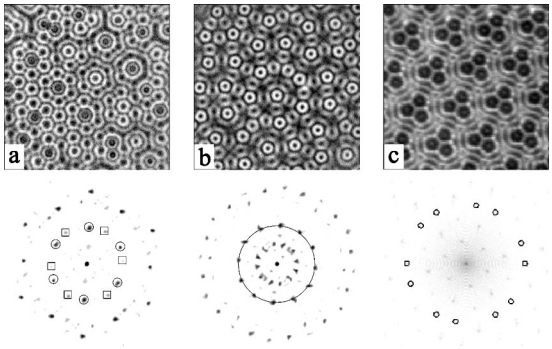

FIG. 18. When using even/odd driving, a class of temporally harmonic states exists that is composed of two distinct hexagonal sublattices (delineated by squares and circles) of size K, the critical wave number of the harmonic driving component. (a) Double hexagon state (DHS) formed by both the critical hexagonal lattice and an additional hexagonal sublattice of smaller amplitude, which is rotated by an angle of ~22°. (b) 12-fold quasicrystalline state. (c) A similar (''SL1'') state observed by Kudrolli, Pier, and Gollub [21] for $\frac{6}{7}$ driving. This state is formed by a resonance similar to (a) but with spatial phase of $2\pi/3$ in each of the sublattice components. (a) and (b) were obtained for $\frac{4}{5}$ ($\frac{60}{75}$ Hz) forcing. (c) was reproduced with permission from [21].

modes can indeed appear. In $\frac{4}{5}$ driving typical SSS-I states with a frequency response of $m\omega_0/4$ are observed far from χ_c. Near χ_c, both the 12-fold temporally harmonic quasicrystalline states first described by Edwards and Fauve [18] as well as a state composed of a *cascade* of symmetry-breaking bifurcations occur. This second type of pattern, which has a subharmonic time dependence, is shown in Fig. 17(a)

This ''cascaded'' state appears as either a secondary bifurcation of an initial hexagon pattern or as a bifurcation from a 12-fold quasipattern state. In its spatial power spectrum the two mechanisms that appeared in both SSS-I- and SSS-II-type patterns are cascaded and appear at different scales. An SSS-II-type resonance occurs where wave vectors $\vec{q}_i$ with magnitudes $q_i = K/\sqrt{3}$ appear. A *third* vector $\vec{Q}$, however, is also present. $\vec{Q}$ is half the magnitude of $\vec{q}_i$ and, echoing the mechanism forming SSS-I states, breaks the sixfold symmetry of the $\vec{q}_i$ by aligning itself parallel to a single vector, $\vec{q}$.

Figure 17(b) demonstrates that this state has an overall temporal periodicity of $2\pi/\omega_0$. The two images [(b) left, right] were taken at an interval of π/ω_0. The images look exactly the same but with a transverse displacement of the $d = 4\pi/K$ length scale. The symmetry breaking by the $\vec{Q}$ is similar to the SSS-I mechanism where a mode with a phase of $\pi/2$ produces a displacive effect, as shown in Fig. 17(b). The peaks are of high amplitude and have the characteristic shape of the oscillons described by Arbell and Fineberg [19] modified by the asymmetry that is produced by the displacive effect of the $\vec{Q}$ mode. In this state different wave vectors are dominant at different temporal phases. These states were not observed in experiments with higher m/n values such as $\frac{6}{7}$ and $\frac{8}{9}$ driving ratios.

V. DOUBLE HEXAGON SUPERLATTICES

Historically, the first two-frequency experiment focused on quasicrystalline patterns with 12-fold symmetry. These were observed in the vicinity of χ_c in systems driven with an even/odd driving ratio and were found to bifurcate either from the flat state or as a second bifurcation from the harmonic hexagon region. In this section we will describe both the 12-fold quasipatterns mentioned above and two other superlattice states (see Fig. 18). All of these states share a harmonic temporal response for odd/even driving and appear in the same general area of phase space. An important factor in pattern selection is the nonlinear coupling coefficient that depends strongly on resonant locking (see Sec. I D 2). In contrast to the SSS states, we will see below that no *new* wave numbers are needed to construct these states. This class of superlattice patterns are differentiated by both the relative angular orientation and spatial phase relations of the critical wave vectors that form them.

The 12-fold quasipattern [see Fig. 18(a)] was observed for $\frac{4}{5}$ driving in the vicinity of χ_c. This state's temporal behavior is harmonic with respect to ω_0. This state can be formed near the linear threshold for small values of $\epsilon \sim 0.01$. Increasing the amplitude A causes a bifurcation to the cascaded-type superlattice described in IV C (see Fig. 17). The 12-fold quasipattern may also be understood as being formed by two

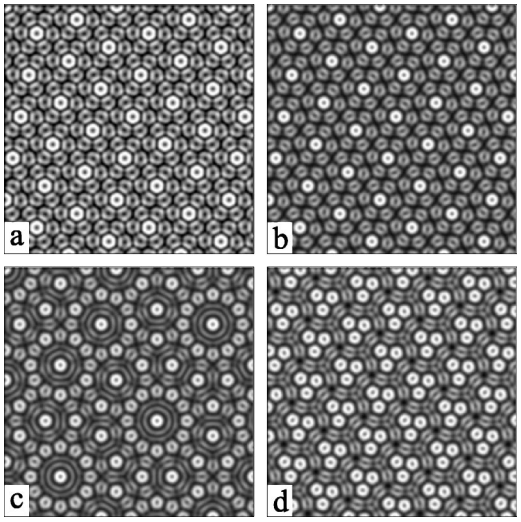

FIG. 19. Using our numerical modeling technique, we calculated the images of a perfect double hexagon state (DHS) formed by two hexagonal lattices rotated by 22°. (a) $\alpha_i=\beta_i=0$ [see Eq. (6)] shows a negative crater state and (b) a positive peak state. (c) shows the calculated image of a 12-fold quasipattern. (d) A calculated DHS state with spatial phases of $\alpha_i=0$ and $\beta_i=2\pi/3$ as in Fig. 18(c).

sets of hexagonal wave vectors at 30° to each other. As in all quasicrystals, this state does *not* have long-range order or a well-defined subunit cell. It is interesting to note that unlike the quasipattern described in [17] that appeared only for $\phi \sim 75°$, the quasipattern we describe exists for $\phi=0°$.

Another superlattice pattern [Fig. 18(c)] that occurs in this regime of phase space was first studied by Kudrolli, Pier, and Gollub with $\frac{6}{7}$ driving ratio with $\omega_0/(2\pi)=16.44$ Hz, $\nu=20$ cS, and $h=0.3$ cm. They found a hexagonal superlattice pattern composed of two hexagonal sets of critical wave vectors with harmonic temporal response. The equation that describes the surface height function of this pattern can be generally written down as

$$h(r)=\sum_{i=1}^{3} A_i \cos(\vec{K}_i\cdot\vec{r}+\alpha_i)+\sum_{i=1}^{3} B_i \cos(\vec{K}'_i\cdot\vec{r}+\beta_i), \tag{6}$$

where $|K|=|K'|=k_c$ and

$$\vec{K}_1=K(1,0),\quad \vec{K}_2=K\left(-\frac{1}{2},\frac{\sqrt{3}}{2}\right),\quad \vec{K}_3=K\left(-\frac{1}{2},-\frac{\sqrt{3}}{2}\right),$$

and $\vec{K}'_i$ can be obtained by rotating $\vec{K}_i$ by an angle of $\theta=22°$. In Figs. 19(a), 19(b) and 19(c) we show simulated images of this equation for different values of β and A_i/B_i.

The pattern [Fig. 18(c)] described by Kudrolli, Pier, and Gollub was found to have an angle θ with the value $\theta=2\sin^{-1}(1/2\sqrt{7})\approx 22°$, equal amplitude coefficients $|A_i|=|B_i|$ for $i=1,2,3$, and spatial phase angles $\alpha_i=0°$ and $\beta_i=120°$. For this special value of θ, resonance conditions such as $2\vec{K}'_1-\vec{K}'_3=2\vec{K}_1-\vec{K}_3$ were shown [21] to exist.

Double hexagon states formed by the superposition of two hexagon sets of critical wave vectors oriented at a relative angle $\theta=2\sin^{-1}(1/2\sqrt{7})$ are one example [23,34] of a wider class of superlattices. This superlattice class is composed of a periodic lattice formed by a wave number smaller than the critical wave number of the excited surface waves. This smaller wave number corresponds to the six wave vectors formed by the difference between adjacent wave vectors of the two hexagonal sets, i.e., by $\vec{Q}_i=\vec{K}_i-\vec{K}'_i$ for $i=1,2,...,6$. Any two of these wave vectors, say $\vec{Q}_1$ and $\vec{Q}_2$, are primitive vectors of the lattice, and the vectors $\vec{K}_i$ and $\vec{K}'_i$ are points on the Q lattice given by $\vec{K}_i=n_1\vec{Q}_1+n_2\vec{Q}_2$. Silber and Proctor [23] show that only a discrete countable set of $\vec{Q}_i$, where $K/Q=\sqrt{n_1^2+n_2^2-n_1n_2}$, can satisfy this condition. The angle θ between the two lattices is given by

$$\theta=\cos^{-1}\left(\frac{n_1^2+2n_1n_2-n_2^2}{2(n_1^2-n_1n_2+n_2^2)}\right).$$

In this formulation the experimentally observed patterns are obtained for $n_1=3$, $n_2=2$, and $K/Q=\sqrt{7}$, giving $\theta\approx 22°$. Only the simplest DHS's have been observed to date.

One characteristic aspect of the DHS's is the relative spatial phase of the different wave vectors. The pattern described by Kudrolli, Pier, and Gollub [21] [coined SL-1, see Fig. 18(c)] consisted of triangular unit cells that were produced by a DHS with $\alpha_i=0°$ and $\beta_i=120°$. Silber and Proctor describe, in simulations of thermal convection, a DHS formed with both $\alpha_i=0°$ and $\beta_i=0°$ [23]. The DHS superlattice in our experiments with a $\frac{2}{3}$ driving ratio [see Fig. 18(a)] differs from these superlattices in that the two hexagonal sublattices that form them possess *different* amplitudes. States similar to these been observed in nonlinear optics [46]. In addition, in our case, there is no spatial phase difference between the two sets of hexagonal wave vectors ($\alpha_i=\beta_j$ for all i, j).

Although this state is stable close to the threshold, increasing the driving amplitude results in the appearance of many defects and eventual temporal disorder. At high driving amplitudes the spatial symmetry is hard to discern due to the many defects and domains within the fluid cell and the state oscillates between a negative amplitude, craterlike phase and a positive amplitude oscillonlike phase with a frequency of ω_0. High-amplitude oscillons appear in the center of the hexagonal subunit cell of the DHS state. Similar oscillons were also observed for the 12-fold quasipattern state shown in Fig. 18(b) [19].

Let us summarize the common characteristics of DHS states. All of the patterns reveal a harmonic time dependence and the lack of any *fundamental* wave vectors other than the critical wave vectors excited by the harmonic frequency. All of these patterns were observed to be in the vicinity of χ_c on the harmonic side. In all cases, the mixing angle was greater than that needed for obtaining SSS states and within the range $\chi_c°>\chi>(\chi_c-12°)$. Another common characteristic of these states is that all exist in the vicinity of a first-order transition of the hexagonal patterns from the featureless fluid state. This implies that quadratic interactions can play an

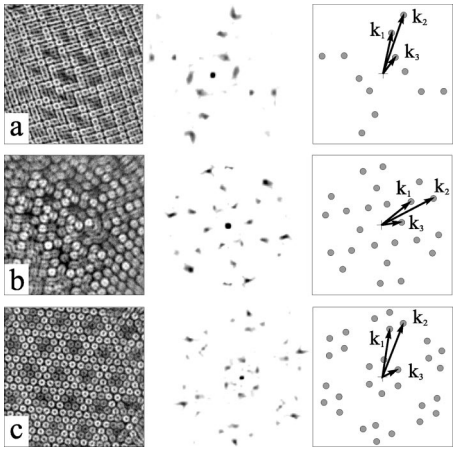

FIG. 20. 2MS patterns consist of a nonlinear superposition of *both* eigenmodes, k_1 and k_2, excited by the driving frequencies ω_1 and ω_2. Although ω_1 and ω_2 determine the lengths of k_1 and k_2, their relative orientations are determined by the condition $\vec{k}_3=\vec{k}_2-\vec{k}_1$, where the wave number k_3 is determined by the temporal resonance condition $\omega_3=\omega_2-\omega_1$. (a) 2MS patterns for $\frac{50}{80}$-Hz driving where k_2 with square symmetry is dominant. (b) k_2-dominant 2MS with hexagonal symmetry for $\frac{45}{60}$-Hz driving and (c) k_1-dominant states having hexagonal symmetry for 40/60 Hz. Shown are the spatial spectra (center) with the resonant triads (right) $\vec{k}_3=\vec{k}_2-\vec{k}_1$, highlighted.

important part in describing these states. Finally, two of these patterns also generate oscillons as described in detail in [19].

VI. TWO-MODE SUPERLATTICES

In the vicinity of the critical mixing angle χ_c two modes with different wavelengths can be excited concurrently. These modes can interact in different ways to produce a variety of different patterns. In the following two sections we will describe two distinct types of two-mode states that are formed near χ_c. The first of these states are two-mode superlattices (2MS). These states are formed by the interaction of the two linearly excited modes with a third ''slaved'' mode that is selected via a temporal resonance.

Figure 20 shows the three main types of 2MS states; k_2 dominated (with either square or hexagonal symmetries) and k_1 dominated (with hexagonal symmetry). 2MS states exist in both harmonic and subharmonic regions of phase space in the vicinity of χ_c (see Fig. 4). In the region of phase space between the square 2MS and the hexagonal 2MS a spatially disordered ''unlocked'' state exists. Unlocked states, which are formed by the same wave numbers that form the 2MS, have no well-defined spatial symmetries. As in the case of SSS states, the transition to 2MS from either square or flat states is nonhysteretic and occurs via propagating fronts.

The 2MS are qualitatively different than SSS states. They result from spatial phase locking of both k_1 and k_2 whereas the SSS states result from a resonance condition that is *independent* of the k_2 mode. 2MS states are the most general of the superlattice states described here. They are observed for all types of driving parities (odd/even, even/odd, and odd/odd) and, as shown in Fig. 20, appear with either square or hexagonal symmetry.

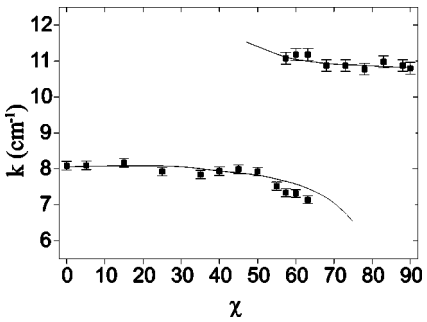

FIG. 21. A comparison of k (in cm^{-1}) calculated using the two-frequency linear calculation [13] (solid line) with measured values of k as a function of χ. Note that both values of k are nearly constant away from $\chi_c=58°$. Near χ_c,k_1 (corresponding to $\omega_1=40$ Hz) decreases by nearly 10% while k_2 (corresponding to $\omega_2=60$ Hz) increases slightly.

A. 2MS Resonance condition

2MS spatial spectra, as shown in Fig. 20, are composed of peaks of length k_1 and k_2 and their linear combinations. The strongest secondary peaks, indicated in the figure, are given by $\vec{k}_3=\vec{k}_2-\vec{k}_1$ where the magnitude of k_3 is consistent with the linear value of k calculated for a single-frequency excitation at the difference frequency $\omega_3=\omega_2-\omega_1$. Our calculated value of k_3 was obtained using the *linear* single-frequency code of [14] at threshold. The difference between the calculated and measured values of k_3 varies between 5% and 20%. This shift between the measured and calculated values is constant for a given value of the difference frequency ω_3 and systematically decreases as ω_3 increases. We believe the shift to be the result of either finite size effects in the cell or the fact that the $\omega(k)$ used is the linear dispersion relation for a *featureless* state (not one with preexisting waves).

A subtle point in the interpretation of the power spectra of 2MS states is the evaluation of the magnitude of the two wave vectors that appear. As can be seen in Fig. 21 the values of k_1 and k_2 measured in the vicinity of χ_c are significantly different than the values of k excited by single-frequency excitation. The two-frequency linear stability code of Tuckerman and co-workers [13,35] reproduces this effect and agrees to within 1–2 % with the experimentally measured values (see Fig. 21). This enables us to accurately calculate values of both k_1 and k_2 in the vicinity of χ_c.

The resonant conditions stated above suggest that the orientation of the wave vectors building the 2MS is selected by nonlinear interactions that are resonant both in space and time. Thus, the temporal resonance condition dictates the spatial orientation of the vectors $\vec{k}_1$ and $\vec{k}_2$. Such three-wave resonant interactions have been predicted to occur in nonlinear interactions of surface waves [47] and are well known in the physics of plasmas. Similar states were observed as a result of nonlinear mixing of a multiple-mode optical beam [48]. The selection of k_3 via the temporal resonance condi-

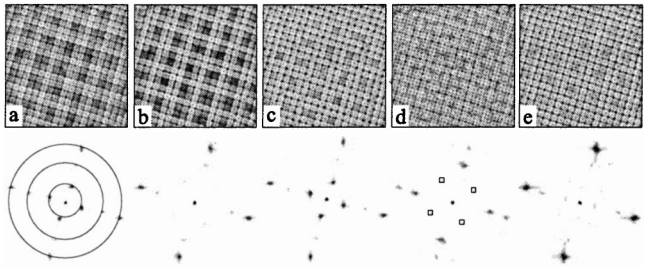

FIG. 22. A typical temporal sequence of square 2MS states taken at constant parameter values for $\frac{50}{70}$-Hz driving. k_1 (middle circle), k_2 (outer circle), and k_3 (inner circle) are indicated in (a). In (d) the k_3 vectors are absent but enclosed in squares are vectors that are the vector sum $\vec{k}_3'+\vec{k}_3$. System parameters are $\omega_0/(2\pi)=20$ Hz, $\nu=23$ cS, $\phi=0°$, $\chi=65.4°$, and $h=0.155$ cm.

tion yielding ω_3 is nontrivial and cannot be accounted for by experimental artifacts such as possible nonlinearities in the imaging. This three-wave resonance condition occurred for *all* frequency ratios tested.

As in SSS, the dominant 2MS wave vector retains its initial symmetry, while the relative orientations of the other linearly excited wave vectors are determined by the above resonance condition. For odd/even driving hexagonal (square) symmetry dominates for $\chi<\chi_c$ ($\chi>\chi_c$). Thus, square 2MS [Fig. 20(a)] bifurcate from the k_2 square pattern that dominates the $\chi>\chi_c$ region. Similarly, hexagonal 2MS [Fig. 20(b)] bifurcate from the k_1 hexagonal pattern that dominates the $\chi<\chi_c$ region. In $\frac{3}{4}$ driving, hexagonal 2MS states are excited whose dominant scale is that of the larger wave number k_2 [Fig. 20(c)]. It is known that in single-frequency driving experiments, different symmetries can arise for different system parameters even when the temporal behavior is solely subharmonic. In two-frequency driving experiments the parity of the dominant frequency does not automatically dictate the symmetry selected. For example, in $\frac{5}{8}$ driving (50/80 Hz), 2MS states are observed with square symmetry in the temporally harmonic region.

B. Temporal behavior of 2MS

Using our strobed imaging technique, we studied the spatiotemporal behavior of the patterns by inspecting them at

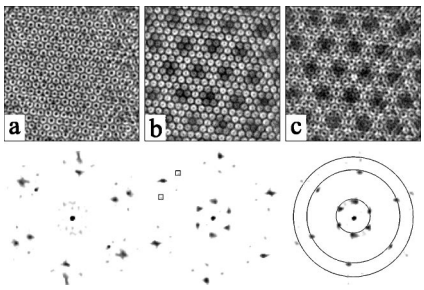

FIG. 23. A typical sequence of *hexagonal* 2MS (a)–(e) at different temporal phases taken at constant parameter values for $\frac{60}{80}$-Hz driving. Circles of radii k_1 (middle), k_2 (outer), and k_3 (inner) are drawn in (c). In (b) the k_3 and k_1 vectors interact to produce the vectors enclosed in squares. k_1 and k_2 form two sets of hexagonally arranged vectors.

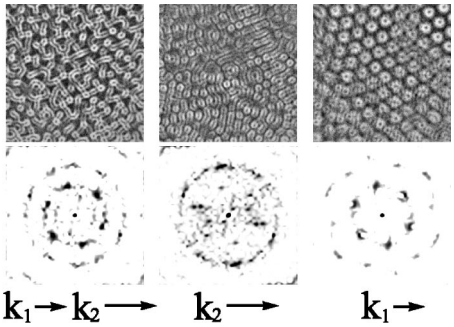

FIG. 24. A typical sequence of k_1 dominant hexagonal 2MS states taken at constant parameter values for $\frac{40}{70}$-Hz driving. These states generally appear in domains. (Wave numbers are noted by arrows.)

different temporal phases. The 2MS inherit the basic temporal periodicity of *both* primary eigenfunctions, which are periodic in time with a basic frequency of either ω_0 (harmonic) or $\omega_0/2$ (subharmonic). The superposition of the two modes always displays a subharmonic response ($\omega_0/2$). Like the SSS, the state's appearance changes qualitatively with time, with the spatial wave numbers having fixed *locations*. 2MS time-dependence stems from the temporal dependence of the *amplitudes* of these modes. In Figs. 22 and 23 we see typical sequences of both square and hexagonal 2MS states taken at constant values of the driving parameters. The relative intensities of the different wave vectors change in the different phases; in Fig. 22(e) the k_1 and k_3 wave vectors are almost absent, resulting in a pattern whose dominant square symmetry has a $2\pi/k_2$ scale, while in the remainder of the phases all vectors appear. In Fig. 23 the resonance condition allows $\vec{k}_1$ and $\vec{k}_2$ to be nearly collinear and two sets of sixfold wave vectors appear in the power spectrum. As in the square 2MS, one can see phases with significantly stronger k_1 peaks [Fig. 23(a)] as well as those where either the k_3 [Fig. 23(b)] or k_2 [Fig. 23(c)] are stronger.

The relative stability of 2MS hexagonal states [e.g., Figs. 20(b) and 20(c)] is dependent on whether k_1 or k_2 is dominant. Let us first consider hexagonal 2MS states where k_1 dominates. This state is found for even/odd driving for $\chi<\chi_c$ (see Fig. 4) and a typical time sequence is presented in Fig. 24. Again, different wave numbers are dominant in different temporal phases. The region of phase space where this state appears is not as large as the k_2 dominant 2MS, but these states appear for all even/odd driving ratios used. As in the case of square 2MS and the $2kR$ states discussed in Sec. VII, these states are not observed for all combinations of ϕ and δ/h used. It is difficult to obtain a hexagonal 2MS state of this kind that extends over the entire system and k_1-dominant hexagonal 2MS states generally occur within domains. Thus the spatial spectra (as seen in Fig. 24) appears sometimes smeared, as the various domains have different angular orientations. Although the scenario described in Fig. 24 is typical, we have observed stable global k_1 dominated 2MS states for particular values of ϕ and δ/h (see, e.g., Fig. 46).

A typical time sequence and power spectra for the k_2 dominant hexagonal 2MS state [shown in Figure 20(c)] is

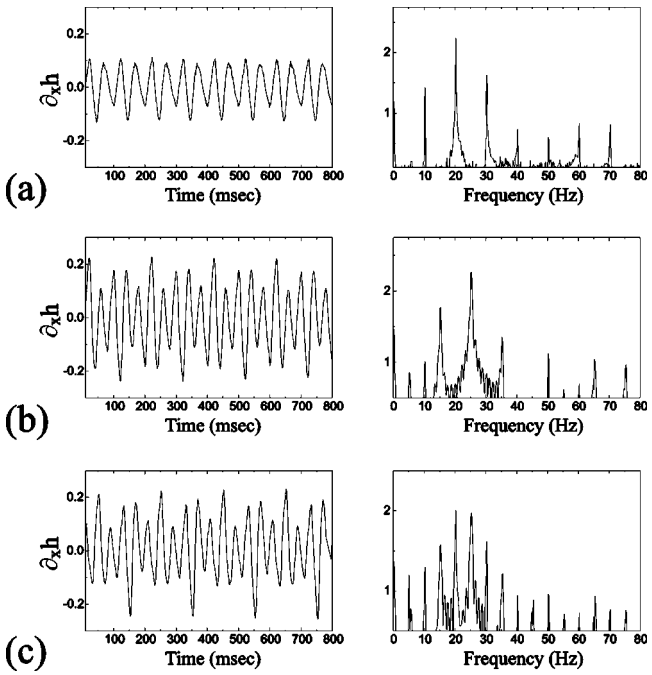

FIG. 25. The time dependence of a two-frequency experiment with even/odd driving was studied using the reflection of a laser by the surface waves. The temporal response is subharmonic (harmonic) with respect to $\omega_0=10$ Hz for $\chi<\chi_c$ ($\chi>\chi_c$). Time series (left) and power spectra (right) for three different regimes. (a) Typical temporal response for hexagonal pattern found for $\chi<\chi_c$. Although the $4\omega_0/2=20$ Hz component is the strongest, an $\omega_0=10$-Hz harmonic component with all of its higher harmonics is present. (b) Typical time dependence for square patterns (found for $\chi>\chi_c$). The strongest response is for $4\omega_0/2=25$ Hz as expected. A weaker response at the basic subharmonic $\omega_0/2=5$ Hz is observed together with stronger responses at other harmonics. The ordering of the harmonics agrees qualitatively with [11]. (c) Typical temporal response of a square 2MS state at χ_c. The power spectrum shows a strong response at both ω_1 (20 Hz) and ω_2 (25 Hz). All other harmonics are present with a different power distribution than in (a) and (b). System parameters here are $\frac{50}{40}$ Hz, $\nu=23$ cS, $h=0.155$ cm, $\phi=0°$, and $\chi=40°$ (a), $\chi=60°$ (b), and $\chi_c=53.5°$ (c).

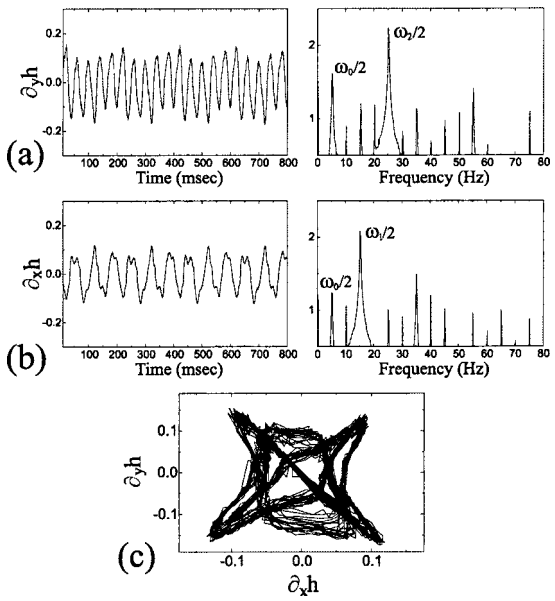

FIG. 26. The time dependence of a square 2MS state measured via the reflection of a laser at the fluid surface. Time series (left) of surface gradients $\partial_y h$ (a) and $\partial_x h$ (b) are shown with their power spectra (right). (c) $\partial_y h$ as a function of $\partial_x h$. The separation of the temporal response (a), (b) was obtained by choosing x and y along the symmetry directions. $\partial_x h$ is dominated by a $3\omega_0/2=15$ Hz response whereas $\partial_y h$ undergoes a $5\omega_0/2=25$ Hz response. System parameters used were $\frac{50}{30}$ Hz, $\nu=23$ cS, $h=0.155$ cm, $\phi=0°$, and $\chi_c=56.3°$.

presented in Fig. 23. Here, in contrast to k_1 dominant hexagonal 2MS, the pattern is global with a well-defined symmetry in all of its temporal phases. Hexagonal symmetry was *not* seen to be preferred for all odd/even driving and was only observed for the simple ratios of $\frac{1}{2}$ and $\frac{3}{4}$. This might be a feature of simple driving ratios that can sometimes have unique properties that are related to temporal locking [11,33].

2MS states are not always as highly ordered as those in Figs. 22 and 23. When highly ordered 2MS states occur, the resonance condition for these parameters allows $\vec{k}_1$, $\vec{k}_2$, and $\vec{k}_3$ to be nearly collinear. When the angles between the resonant wave vectors are not small the pattern is usually not global and a number of domains coexist. In highly ordered states we find a locking of the wave vectors' magnitude to small natural number ratios. The locking ratios of $k_1:k_2:k_3=1:3:4$ and 1:4:5 were, respectively, obtained in Figs. 22 and 23. This ''spatial locking'' seems to stabilize global patterns in a way similar to the global SSS states presented in Sec. III.

The local laser probe technique provides more detailed, quantitative information of the temporal behavior of 2MS states. In Fig. 25 we show one component of the slope of surface waves obtained for $\frac{4}{5}$ driving. In Fig. 25(a) we show the typical wave form of a hexagonal pattern for $\chi<\chi_c$. Besides the strong component at $\omega_1/2=4\omega_0/2$ and its harmonics 40,60,80, . . . (in Hertz), peaks appear at values of $j\omega_0$, $j=1,2,\ldots$. Those peaks are expected from the linear theory. In Fig. 25(b) we see a typical wave form of a square pattern for $\chi>\chi_c$. Although the strongest frequency response is at $\omega_2/2$, the basic frequency $\omega_0/2$ together with its higher harmonics also appear. Linear theory predicts a different distribution of energy in the peaks for the unstable mode at threshold. Zhang and Vinals's [11] nonlinear theory accounts for the peak's strength in a semiquantitative way, as it correctly predicts the ordering of the strongest peaks.

In Fig. 25(c) the temporal response of the 2MS state is presented. This state has a temporal response that includes both the frequencies of the harmonic mode, (a) for $\chi<\chi_c$, and those of the subharmonic one, (b) for $\chi>\chi_c$. Although the power spectrum shows that both main peaks at $\omega_1/2$ and $\omega_2/2$ are of the same strength, their relative strengths can vary with the location of the laser probe.

We have seen that the 2MS state contains the two linearly excited eigenmodes both in space and in time. Does each mode keep its distinct space-time behavior, or is there a com-

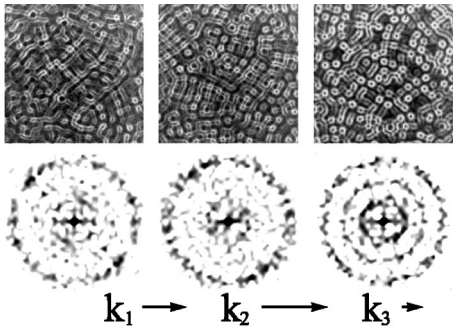

FIG. 27. In the ''unlocked'' state no orientational order is apparent. As in 2MS states, k_1, k_2, and k_3 exist simultaneously but unlocked state spectra are diffuse and show little angular correlation. Top: Typical views of an unlocked state with corresponding spatial spectra (bottom) observed for $\frac{40}{60}$-Hz driving at different times and fixed driving parameters. The different values of k appear with different magnitudes and orientations in each phase. Their lengths are indicated by the arrows.

plete mixing of the spatial and temporal components? To clarify this question, we write down a simple model for the surface height of a square 2MS state. For simplicity, we will assume a square 2MS state where both $\vec{k}_1$ and $\vec{k}_2$ are collinear with the same spatial phase,

$$h(r,t)=F_1(t)[\cos(k_1x)+\cos(k_1y)]+F_2(t)[\cos(k_2x)+\cos(k_2y)], \tag{7}$$

$$\frac{\partial h}{\partial x}=k_1F_1(t)\cos(k_1x)+k_2F_2(t)\cos(k_2x),$$

$$\frac{\partial h}{\partial x}=k_1F_1(t)\cos(k_1y)+k_2F_2(t)\cos(k_2y),$$

where $F_1(t)\sim\cos(\omega_1t/2)+\cdots$ and $F_2(t)\sim\cos(\omega_2t/2)+\cdots$. It is easily seen that if one selects a point $(x,y)=(\pi/2k_2,\pi/2k_1)$ then each of the components of the partial derivative $\partial h/\partial x$ and $\partial h/\partial y$ has a temporal dependence of $F_1(t)$ and $F_2(t)$, respectively. Both $F_1(t)$ and $F_2(t)$ include time dependent terms retaining the parity of the linear modes: odd multiples of $(p+\frac{1}{2})\omega_0$ for a subharmonic response and even multiples of $p\omega_0$ for a harmonic response.

As suggested by Eq. (7), experiments (see Fig. 26) confirm the separation of the time dependence of the two modes within the 2MS state. The $\partial_x h$ component has a strong $\omega_1/2$ response whereas the $\partial_y h$ component's strongest peak is at $\omega_2/2$. This strong separation of spatial time dependencies can only be observed for a few points in the (x, y) plane and, in general, the two frequencies are mixed.

C. The "unlocked" state and transition regions

Let us now consider the ''unlocked'' state that appears in the near vicinity of χ_c. In Fig. 27 we present a typical time series of the unlocked state and its corresponding spatial spectra. The spatial behavior of the state varies rapidly over time scales of order $(2\pi/\omega_0)$. In contrast to the SSS and

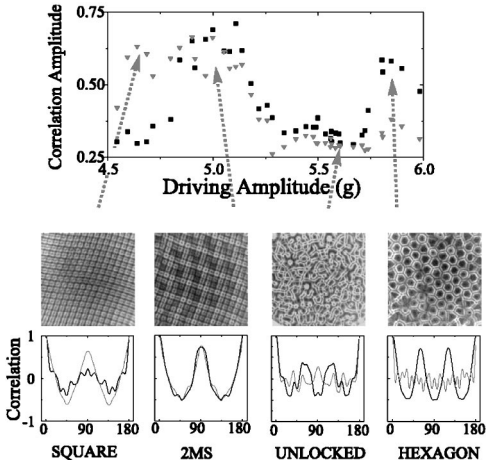

FIG. 28. Within the ''unlocked'' states, the correlation amplitude Q_k drops significantly and the angular correlation function $C_k(\theta)$ indicates only a small amount of residual order. Top: Q_{k_1} (triangles) and Q_{k_2} (squares), averaged over a single period along the line $\chi=58°$ for $\frac{40}{60}$-Hz driving as a function of the driving amplitude A. This line traverses the square, square-2MS, unlocked, and hexagonal-2MS phases. Typical patterns in each phase are displayed (center). The symmetry of the different phases is highlighted by $C_k(\theta)$ for k_1 (gray line) and k_2 (black line) computed for typical states (θ is in degrees). The power (log scale) of k_2 relative to k_1 in each $C_k(\theta)$ is 8.3 (square), 1.1 (2MS), 0.9 (unlocked), and 0.2 (hexagon).

2MS states, in the unlocked state no orientational order is apparent. Both k_1 and k_2 exist simultaneously in their spatial spectra but spatial mode locking does not occur as in the 2MS states. This is evident in their power spectra, where, generally, entire circles of radii k_1 and k_2 appear. As Fig. 27(d) indicates, additional peaks of wave number k_3 corresponding to $\omega_3=\omega_2-\omega_1$ are sometimes observed. The unlocked state is a well-defined state that exists in a relatively wide region of phase space. This can be seen by defining (as in [2,15]) the following ''orientational correlation function,'' $C_k(\theta)$ for each value of k:

$$C_k(\theta)\equiv\sum_\alpha[f_k(\alpha)f_k(\alpha+\theta)]\Big/\sum_\alpha[f_k(\alpha)f_k(\alpha)], \tag{8}$$

where $f_k(\alpha)$ is the Fourier transform of the wave number k

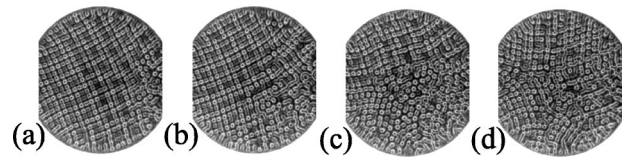

FIG. 29. The transition between the square-2MS state and the unlocked state occurs through a gradual process in which both states coexist in different domains. At the transition, increasing the amplitude for constant χ constant result in (a) the global 2MS state which is first disturbed by small defects at the cell's rim. (b), (c) The disturbance spreads to the cell's center until, finally, the entire pattern is in the unlocked state shown in (d). This process can also occur in the reverse direction. The spatial scale is given by the 14.4 cm cell diameter.

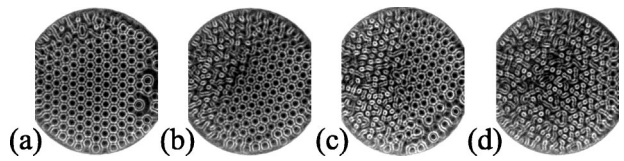

FIG. 30. A time sequence of the transition from the regular hexagonal state (a) to hexagonal-2MS states is shown. The k_2 (60-Hz) component propagates via a front (b), (c) until it dominates the entire plate and coexists with the large length scale (d). The driving parameters are constant for this sequence. The spatial scale is given by the 14.4 cm cell diameter.

at the polar angle α. The correlation amplitude, $Q_k = \frac{1}{2}[\max C_k(\theta) - \min C_k(\theta)]$, varies between 0 and 1 for, respectively, minimal and maximal orientational order. As Fig. 28 shows, both the 2MS and hexagonal states have clear orientational order while very little residual order is apparent in the unlocked state.

As is apparent from Fig. 28, the orientational amplitude drops sharply as the boundary between the 2MS and unlocked phases is crossed. This is demonstrated in Figs. 29(a)–29(d), which corresponds to the range of 5.1–5.25 g in Fig. 28. Between the pure hexagonal state and the unlocked state the hexagonal 2MS state exists. This state displays strong k_1 dominant hexagonal symmetry at most temporal phases but at other temporal phases some of the power is in the k_2 mode. Since Q_k is an average of equally time separated temporal phases, the hexagonal 2MS state has a Q_k that is slightly smaller than that of the pure hexagon state.

The parameter Q_k does not completely characterize the different transitions, since spatial fast Fourier transform power spectra cannot differentiate between global and local ordering. A closer look at real-space images of the transitions presented in Fig. 28 that correspond to square-2MS, unlocked, and hexagonal-2MS states are shown, respectively, in Figs. 29 and 30. Both transitions involve an advancing front that separates two well-defined domains. The clear separation between unlocked and 2MS domains provides further evidence that the unlocked state is indeed a distinct nonlinear state and not, simply, a transition region.

The transitions between unlocked states and the 2MS states with different symmetries differ in two ways. The sensitivity to any change of the driving parameters is much higher for the unlocked to 2MS-hexagon transition. Whereas the transition between square 2MS and unlocked states occurs for a relative change of amplitude of less than 5%, the transition between hexagonal-2MS states and hexagons can occur via a change smaller than 0.25%. The time scales of the induced transitions are also different. The first transition takes place in a nearly quasistatic reversible way, whereas the second transition (as shown in Fig. 30) can occur over typical time scales of 50–1000 oscillation periods with a hysteresis of less than 0.1%. This rather sharp transition is, perhaps, due to the effects of the quadratic interactions inherent in the harmonic states. The precise duration of this transition depends on the initial and final driving parameters. As is typical of front propagation processes, the deeper one is within the hexagonal regime, the faster the transition time [49].

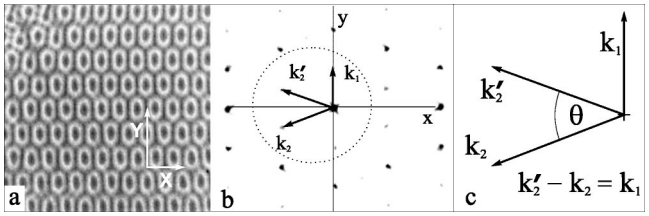

FIG. 31. (a) A typical $2k$ rhomboid ($2kR$) state observed for $\frac{2}{3}$ driving and $\omega_0/(2\pi) = 25$ Hz, $\nu = 23$ cS, and $h = 0.2$ cm. The axis y is defined by the direction of k_1. (b) The power spectrum (c) illustrates the simple resonance condition $\vec{k}_2' - \vec{k}_2 = \vec{k}_1$ that generates these states. $\vec{k}_2'$ and $\vec{k}_2$ correspond to $\omega_2 = 3\omega_0/2$ while $\vec{k}_1$ corresponds to $\omega_1 = 2\omega_0/2$. θ here is 41°.

VII. RHOMBOIDAL STATES ($2kR$) AND QUASIPATTERNS

In the preceding section we studied the three-wave resonance mechanism that can form 2MS states from the interaction $\vec{k}_3 = \vec{k}_2 - \vec{k}_1$ and $\omega_3 = \omega_2 - \omega_1$. Are the only resonant mechanisms found in the vicinity of χ_c?

In this section we will describe the spontaneous formation of nonlinear rhomboidal patterns, formed as a result of solely *spatially* resonant three-wave coupling between wave vectors with distinctly different wave numbers. This state has previously been observed only in a nonlinear optical system where the orientations of the interacting wave vectors [50] were externally imposed. Rhomboidal patterns have also been recently observed in parametrically driven ferrofluids [44]. The rhomboidal patterns described below spontaneously couple the two circles of linearly degenerate wave numbers. These states qualitatively differ from 2MS states in that they are composed solely of the linearly excited wave vectors k_1 and k_2, in contrast to the additional slaved mode k_3 necessary for 2MS formation.

The rhomboidal states observed in this system result from the nonlinear interaction of k_1 and k_2, which are waves with significantly different wavelengths. Such states have been observed numerically in a Swift-Hohenberg-type models [25,27] as discussed in Sec. I. They have also been anticipated in anisotropic models where two degenerate wave vectors are resonant with an externally imposed wave number [51], in nonlinear optical systems [52,53], and in the analysis of the Faraday instability excited with two frequencies [30,33]. Both rhomboidal states and superlattice patterns have also been recently predicted to occur as a result of two bistable modes coupling to a zero mode [54].

The rhomboidal states observed in this system differ distinctly from rhomboids resulting from slightly ''distorted'' hexagonal states [55,56]. ''Distorted hexagons,'' predicted to be stable in models with derivative-coupled quadratic terms, may arise due to either initial or boundary conditions [57]. These states have been observed in reaction-diffusion systems [56], convection in an imposed shear flow [58], and flux line lattices in superconductors [59].

A. Experimental conditions

We have observed rhomboid states using both Dow-Corning 200 oils with kinematic viscosities ν of 8.7, 23, 47,

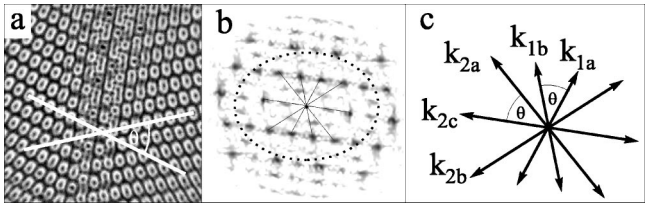

FIG. 32. A common phenomenon observed in the $2kR$ region of phase space is the formation of two domains of $2kR$ states (left) that are oriented with a relative angle of θ that is also the angle between the two larger vectors $\vec{k}_2$, $\vec{k}_2'$ forming the $2kR$ state. A similar phenomenon can also be observed in domains formed by triblock copolymers [60].

and 87 cS (at 30 °C) and the TKO-77 vacuum pump fluid with $\nu=184$ cS (at 33 °C) in fluid layers whose depth varied between $0.1<h<0.55$ cm. The two wave number rhombic ($2kR$) states described in this section were all generated with $m/n=2/3$ and $12<\omega_0/2\pi<45$ Hz or $m/n=4/5$ with $10<\omega_0/2\pi<20$ Hz. Frequency combinations of $\frac{25}{50}$, $\frac{30}{60}$, $\frac{40}{80}$, $\frac{40}{56}$, $\frac{45}{63}$, $\frac{48}{68}$, $\frac{50}{70}$, $\frac{55}{75}$, $\frac{55}{77}$, $\frac{30}{50}$, $\frac{40}{70}$, $\frac{45}{60}$, $\frac{50}{65}$, $\frac{50}{80}$, $\frac{52}{68}$, $\frac{60}{84}$, $\frac{60}{100}$ did *not* generate $2kR$ states.

In Fig. 31 we present a typical image of a $2kR$ pattern. Although k_1 and k_2 are the linearly unstable wave numbers [14] excited by ω_1 and ω_2, their orientation is determined by the three-wave nonlinear interaction that yields the resonant triad $\vec{k}_2'-\vec{k}_2=\vec{k}_1$, where $|\vec{k}_2'|=|\vec{k}_2|=k_2$. The higher harmonics in the figure may either be real or could occur as an artifact of the imaging. An additive three-wave resonance occurs for $\frac{1}{2}$ forcing where the resonance $\vec{k}_1'+\vec{k}_1=\vec{k}_2$ governs the selected pattern. In this case, the resulting pattern (see Sec. VIII) is a superposition of hexagonal lattices composed of the two scales.

The observation of $2kR$ states solely for driving ratios $\frac{2}{3}$, $\frac{4}{5}$, and $\frac{1}{2}$ is entirely consistent with Silber and Skeldon's [30] predictions (see Sec. I D 2) that three-waves interactions coupling the wave numbers k_1 and k_2 are only allowed when two odd-parity waves are coupled to a wave with even parity. Thus, $\vec{k}_1'+\vec{k}_1=\vec{k}_2$ coupling is allowed for odd/even frequency ratios such as $\frac{1}{2}$, and $\vec{k}_2'-\vec{k}_2=\vec{k}_1$ coupling occurs in even/odd forcing, such as $\frac{2}{3}$ and $\frac{4}{5}$. It is interesting that we have not observed these states for other frequency ratios. It is possible that 2MS states are preferred for all but the simplest frequency ratios since, for higher ratios, linearly stable tongues corresponding to wave numbers close to the value of k_3 (defined by $\omega_3=\omega_2-\omega_1$) are more dense.

A typical phase space in which $2kR$ states are observed is presented in Fig. 4 (right). For values of χ that are far from χ_c, the phase diagram is similar to those described in Secs. III and VI. The $2kR$ state exists in the near vicinity of χ_c and replaces both the 2MS and unlocked states. This region is bounded for $\chi>\chi_c$ by squares and for $\chi<\chi_c$ by k_1-dominant DHS that are mixed with oscillons [20] (see [19]). At higher values of ν and h (e.g., $\nu=47$ cS, $h=0.3$ cm, $\nu=87$ cS, $h=0.5$ cm) square and hexagonal patterns only exist near onset. Upon increase of A both types of patterns become rolls. The $2kR$ state is, however, unaffected by the state preceding it. They appear for a similar range of ϕ. The transition to DHS and oscillon states also occurs as in Fig. 4.

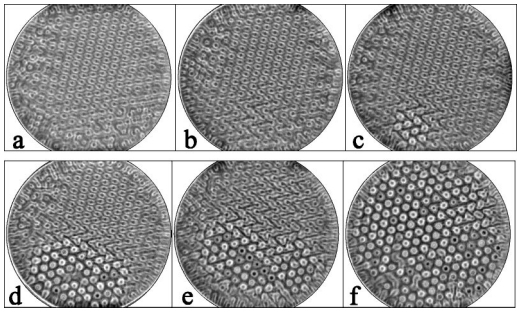

FIG. 33. The transition from the $2kR$ state to the DHS occurs through an "explosive" process in which a spatial domain of hexagons forms and rapidly increases in size. Six images (a)–(f) of this process taken at 1.5-sec intervals for an experiment performed with $\frac{66}{44}$ Hz driving for $\nu=23$ cS and $h=0.2$ cm at mixing angle $\chi=70°$. Note areas of mixed $2kR$ and hexagonal domains around the perimeter of the hexagonal area [clearly seen in upper half of (e)]. In this process the driving parameters are *fixed*. The spatial scale is given by the 14.4 cm cell diameter.

$2kR$ states are not always correlated throughout the entire system. At relatively low values of A, $2kR$ states can sometimes be found in two or three domains, as shown in Fig. 32. The angle separating two such domains is identical to the angle θ between $\vec{k}_2$ and $\vec{k}_2'$, as defined in Fig. 31(b). This type of domain separation is also observed in "knitting patterns" [60], formed by triblock copolymers near a bistable point. (These new materials have a reciprocal lattice structure similar to $2kR$ states.)

Let us return to the description of the typical phase space. As increasing the driving amplitude A strengthens the nonlinear interactions between the waves, $2kR$ domains coalesce at higher levels of excitation. Further increase of A yields a hysteretic bifurcation to the double hexagonal superlattice state, where oscillons are formed at the maxima of the pattern (see [19]). In Fig. 33 we present a time sequence of the transition from a global $2kR$ state to a DHS state by means of rapid front propagation. Only at the final stages of this process does the pattern bifurcate into the high-amplitude state consisting of oscillons superimposed on a DHS background (see Sec. V and [19]). The opposite transition from the DHS to the $2kR$ state has a qualitatively different character. Small k_2 dominated wavelength domains penetrate the DHS from the perimeter of the cell in a way similar to the transition from hexagons to SSS. The transition is not reversible and can have a small hysteresis (under 1%).

Both 2MS and $2kR$ states are observed for the driving ratios $\frac{2}{3}$ and $\frac{4}{5}$. In [22] the dimensionless parameter $\delta/h\equiv(\nu/\omega_{\rm ave})^{1/2}/h$ [where $\omega_{\rm ave}\equiv(\omega_2-\omega_1)/2$] was shown to govern the selection between the two patterns. For $\phi=0$, 2MS/unlocked states exist above $\delta/h\sim0.12-0.17$, while $2kR$ states exist below. This critical range of δ/h was obtained for a broad range of both h ($0.1\leqslant h\leqslant0.6$ cm) and ν ($8.7\leqslant\nu\leqslant186$ cS). The parameter δ/h is the ratio of two important physical scales of the system: the ratio of the viscous boundary layer length, where the flow is rotational, to

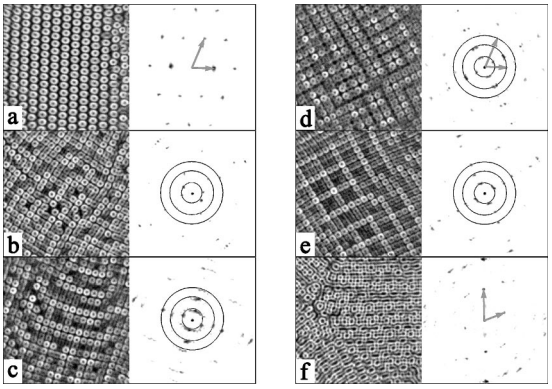

FIG. 34. The effect of changing ϕ in the driving can be seen in the sequence of images (left) and their power spectra (right) for different values of ϕ. While for $\phi=0°$ (a) a $2kR$ state is stable and global, increasing ϕ from (b) 20° and (c) 30° transforms the system to a stable 2MS state at (d) 90°. Increasing the angle to (e) 120° and (f) 150° reverses the process and finally for $\phi=180°$ a global $2kR$ reemerges. The three concentric circles indicate the magnitude of the three 2MS wave vectors (k_1,k_2,k_3), while the gray arrows indicate the wave vectors of the $2kR$ state $\vec{k}_1$, $\vec{k}_2$. These measurements were performed for $\frac{2}{3}$ driving with system parameters $\omega_0/(2\pi)=25$ Hz, $\nu=23$ cS, and $h=0.2$ cm at mixing angle $\chi=70.5°$.

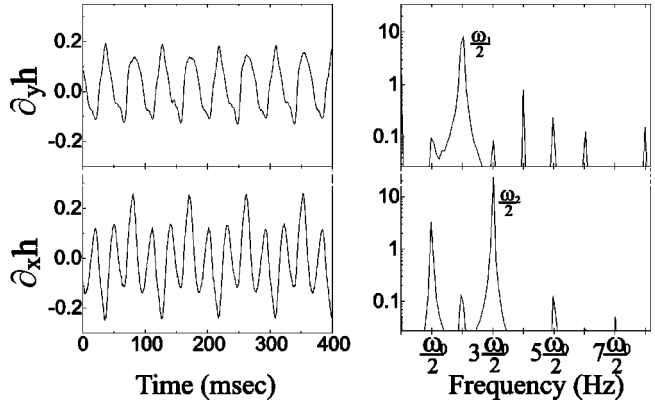

FIG. 35. The time dependence of the $2kR$ state was studied using the reflection of a laser by a point on the fluid surface. The directional derivatives $\partial_x h$ and $\partial_y h$ as a function of time (left) and their corresponding power spectra (right) show that each direction has a different temporal dependence. [The *x, y* directions are defined in Fig. 31(a).] $\partial_y h$ is dominated by the k_2 and k_2' components with dominant frequency $\omega_2/2$, and $\partial_x h$ corresponds to the k_1 component with dominant frequency $\omega_1/2$. This figure was taken from [22]. The parameters for the above were $\omega_0/(2\pi)=22$ Hz, $\nu=23$ cS $\phi=0°$, and $h=0.2$ cm.

the fluid layer's height. This parameter, in essence, defines the region of applicability of Zhang and Vinals's quasipotential approximation. $(\delta/h)^2$ is the ratio of the dissipative time to the driving time scales. In the study of Lioubashevski and co-workers, this number was critical for determining pattern selection by single-frequency excitations [39,36]. Thus, this transition suggests that high dissipation in the system favors the 2MS over the $2kR$ states. This may result from the (linear) broadening of unstable tongues [35] that occurs when dissipation in the system is increased. This broadening would make the linearly stable wave number observed in 2MS states, k_3, more accessible.

In the transition regime of δ/h, both 2MS and $2kR$ states can coexist for $\delta/h=0.12$. In this region, at fixed values of δ/h, small changes in either A or χ can result in globally stable states of either type. Transient states in which both states are present can also result in this regime. In these states both resonant mechanisms can operate *concurrently* in different spatial regions of the fluid cell.

As the two driving frequencies are commensurate, the phase variable ϕ in Eq. (1) is a relevant control parameter. As was shown in the experimental work of Muller and Edwards and Fauve (see Sec. I C) changing ϕ can affect pattern selection. Typically, the $2kR$ state exists over the range $-20°<\phi<+15°$. The phase space presented in Fig. 4 (right) is typical for $0.16<h<0.22$ cm and $\nu=23$ cS. In Fig. 34 we show how changing the angle ϕ causes the pattern to change from the $2kR$ to the 2MS state. The transition is not abrupt and in some regions localized patches of both states can coexist. In general, the size of the region in phase space where a single $2kR$ domain exists decreases with the distance from $\phi=0°$. Because $\phi=180°$ is equivalent, for $\frac{2}{3}$ driving, to $\phi=0°$, the $2kR$ is also stable at this angle. The strong effect of changes in ϕ is consistent with the predictions of Zhang and Vinals (see Sec. I D 1) who showed how ϕ can affect the mode coupling function $\beta(\theta)$. Silber, Topaz, and Skeldon [33] have recently demonstrated that changing ϕ affects the $2kR$ resonance by varying the nonlinear coefficients of the model equations describing the system.

B. Temporal behavior

The temporal behavior of the $2kR$ state is similar to that of the even/odd 2MS states, where the time dependence in different directions is qualitatively different. Like the even/odd 2MS states, different directions can have dominant subharmonic or harmonic components. A time translation of π/ω_0 shifts the observed pattern by a spatial translation of $\pi/|\vec{k}_2+\vec{k}_2'|$ in the x direction [as defined in Fig. 31(a)]. The overall spatiotemporal behavior of the $2kR$ state is consistent with Eq. (9),

$$h(t,x,y)=[a_1\cos(\omega_0 t)+a_2\cos(2\omega_0 t)+\cdots]\cos(\vec{k}_1\cdot\vec{x}) +[b_1\cos(\omega_0 t/2)+b_2\cos(3\omega_0 t/2)+\cdots] \times[\cos(\vec{k}_2\cdot\vec{y})+\cos(\vec{k}_2'\cdot\vec{y})]. \quad (9)$$

The fact that the two directions $\vec{x}\|\vec{k}_1$ and $\vec{y}\perp x$ (as defined in Fig. 31) each exhibit *different* time dependence is demonstrated in Fig. 35. This typical time series of the x and y components of the surface gradient of this state at a single point is similar to that presented in Fig. 26 for the 2MS state. By our choice of axes, the $\partial_x h$ component contains mainly the $\omega_1/2,2\omega_1/2,\ldots$ peaks, while the dominant frequencies in the y direction are $(\omega_2-\omega_1)/2,\omega_2/2,\ldots$. Arbitrary $\vec{x}$ and $\vec{y}$ directions will contain both k_1 or k_2 eigenmodes. This orientational dependence may prove to be a general charac-

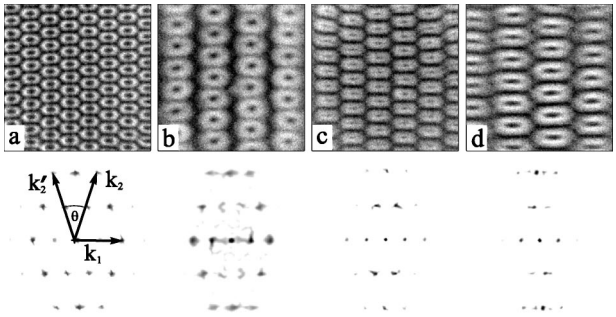

FIG. 36. The resonant angle between k_2' and k_2 varies with the parameters of the experiment. We obtain angles of (a) 36° for system parameters of $\omega_0/(2\pi)=25$ Hz, $\nu=47$ cS, and $h=0.25$ cm; (b) 33° for system parameters of $\omega_0/(2\pi)=15$ Hz, $\nu=87$ cS, and $h=0.5$ cm; (c) 32° for system parameters of $\omega_0/(2\pi)=25$ Hz, $\nu=87$ cS, and $h=0.5$ cm; and (d) 29° for system parameters of $\omega_0/(2\pi)=20$ Hz, $\nu=184$ cS, and $h=0.54$ cm. All images were taken from a 9×9 cm^2 square in the center of the circular plate.

teristic of superlattice states. When a *single* mode is dominant, the predictions of Zhang and Vinals [11] are in good quantitative agreement with our measurements of the relative peak intensities. In the vicinity of χ_c, when two modes are concurrently excited, this analysis does not apply and a new theoretical framework is needed.

In low viscosity fluids ($\nu=8.7$ cS, $0.1<h<0.2$ cm, and $\delta/h<0.13$) an interesting variant of the pure $2kR$ state is observed whose symmetry changes with its temporal phase (see [22]). At different temporal phases, pure hexagonal, mixed hexagonal, and $2kR$ phases can be seen. Interestingly, this state exists for a significantly broader range of ϕ ($-70°<\phi<70°$) than the pure $2kR$ state. Together with the vector triad characteristic of $2kR$ states, coupling with the difference vector, $\vec{k}_2-\vec{k}_1$, is also observed in the spatial spectra of these states.

C. Tuning of the resonant angles and quasipattern formation

The angle θ between the two wave vectors $\vec{k}_2$ and $\vec{k}_2'$ can be tuned by changing the different system parameters. Since the values of k_1 and k_2 are roughly determined by the dispersion relation $\omega(k)$, the angle θ can be varied by changing

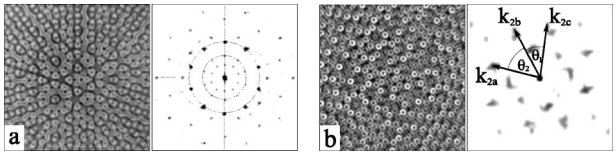

FIG. 37. (a) A tenfold quasiperiodic pattern and its power spectrum is observed for $\omega_0/(2\pi)=30$ Hz, $\nu=47$ cS, and $h=0.33$ cm. Circles are drawn with radii k_1 (inner) and k_2 (outer). For these parameters $\theta=360°/10$ and five $2kR$ regions combine to form the quasipattern. For $\omega_0/(2\pi)=30$ Hz, $\nu=23$ cS, and $h=0.2$ cm (b) a nearly eightfold symmetric pattern is seen. This pattern, however, is actually a deformed quasipattern since the $2kR$ value here of $\theta=41°$ does not evenly divide 360°. Instead of a single angle, two different angles $\theta_1=41°$ and $\theta_2=49°$ are observed in the power spectrum.

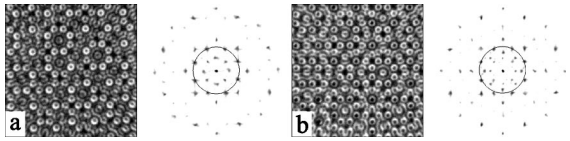

FIG. 38. Two temporal phases of an eightfold quasipattern observed for three-frequency driving (a), (b). This state is temporally subharmonic and was observed in the region where the distorted eightfold quasipatterns were observed (see Fig. 37). This state was observed in a 50/75/100 Hz experiment with driving amplitude ratio $a_1:a_2:a_3$ equal to 0.16:0.36:0.48 and a phase difference of 180° between the 100-Hz component and the two other components.

ω_0, ν, or h while leaving m/n constant. This is demonstrated in Fig. 36. The value of θ can be calculated for a specific mixing angle χ using the numerical method developed by Tuckerman and co-workers [13].

As suggested by [25,26], when rhomboidal states exist, the tuning of θ can provide a well-defined mechanism in which quasipatterns of any desired symmetry may be formed. When $360/\theta=p$, an integer number of adjacent triads can be formed. As conjugate pairs of triads are always formed, the integer p must always be even (as observed in [16,27]). This is demonstrated in Fig. 37 where the formation of perfect tenfold quasicrystalline patterns and approximate eightfold quasipatterns occurs for values of θ that are tuned to these resonant ($360/\theta=n$) angles. As the power spectra of these states indicate, each of the inner circle of peaks of magnitude k_1 is coupled by a triad resonance with two peaks of magnitude k_2 along the outer circle. When $\theta\approx41°$, a symmetric quasipattern is not possible and a distorted eightfold quasipattern, as shown in Fig. 37(b), occurs.

D. Three-frequency driving

Having observed the distorted eightfold quasipatterns described in Fig. 37(b), we attempted to stabilize these *asymmetric* quasipatterns by modifying the driving. Muller in [12] added a third frequency perturbation to break the spatial phase symmetry in the subharmonic regime and thereby control the transition between triangles and hexagons. This motivated us to add a third frequency in order to enable the excited wave vectors k_1 and k_2 to spatially lock to the value of $\theta=45°$ for which eightfold quasipatterns can naturally form. We used the following driving function:

$$A[a_1\cos(p_1\omega_0 t)+a_2\cos(p_2\omega_0 t+\phi_1)+a_3\cos(p_3\omega_0 t+\phi_2)], \tag{10}$$

where the total driving amplitude is given by A and the normalized amplitude ratios by $a_1:a_2:a_3$ with $a_1+a_2+a_3=1$. $p_1:p_2:p_3$ is the three-frequency ratio $p_1<p_2<p_3$ and ϕ_1, ϕ_2 are the phase differences with respect to the p_1 components.

Using 2:3:4 driving we indeed observed a perfect eightfold quasipattern. In Fig. 38 we show images and power spectra of this state at two temporal phases. This state is subharmonic in time and can be observed in the region where tenfold quasipatterns and eightfold distorted quasipatterns were observed for the $\frac{2}{3}$ experiments described above.

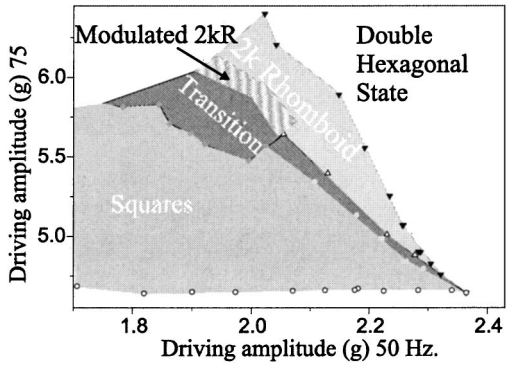

FIG. 39. An expanded view of the phase space described in Fig. 4 (right). Transition states between square and $2kR$ states are formed by a superposition of a square state with one (two) sets of $2kR$ triad vectors. Between the $2kR$ and transition states, a modulated $2kR$ state exists in which an additional $\vec{k}_2$ component parallel to the $\vec{k}_1$ component exists.

Interestingly, this state was exceedingly stable and existed within a single domain over a wide range of parameters (note the sharp peaks in Fig. 38). This is in sharp contrast to the distorted eightfold state shown in Fig. 37, which existed in both a narrow range of parameters and, as evident in its diffuse spectrum, had a tendency to break up into domains. It is possible that the third frequency allows the $2kR$ mechanism to form the quasipattern through the relaxation of the ratio between $\vec{k}_1$ and $\vec{k}_2$ and thereby the angle between them. This state was observed in a 50/75/100 Hz experiment with ratios of driving amplitudes $a_1{:}a_2{:}a_3$ equal to 0.16:0.36:0.48, where the single-frequency critical accelerations for these frequencies are, respectively, $2.56g$, $4.40g$, and $6.91g$ (yielding ratios of 0.18:0.32:0.49) and phase differences $\phi_1=0°, \phi_1=180°$. Although the third frequency acceleration is not small here, it is still below the critical value for single-frequency excitation at 100 Hz, and wave vectors corresponding to the 100-Hz component were not observed.

E. Transition states to rhomboids

Figure 39 shows an expanded view of the $2kR$ phase space around χ_c [see Fig. 4 (right)]. The region shown lies in

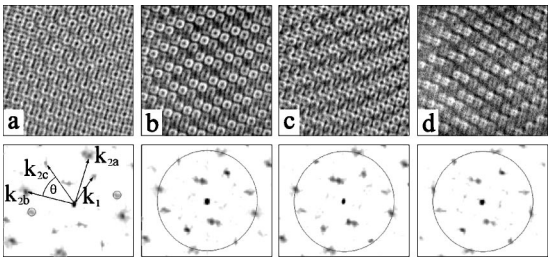

FIG. 40. A typical time sequence of the transition state is shown with the corresponding power spectra (bottom). The wave vectors $(\vec{k}_{2a},\vec{k}_{2b})$ generating the squares appear together with a third wave vector $\vec{k}_{2c}$, which is oriented at an angle of $\theta=41°$ to $\vec{k}_{2b}$. The above experiment was made for system parameters of $\omega_0/(2\pi)=27$ Hz, $\nu=23$ cS, $\phi=0°$, $\chi=69°$, and $h=0.2$ cm.

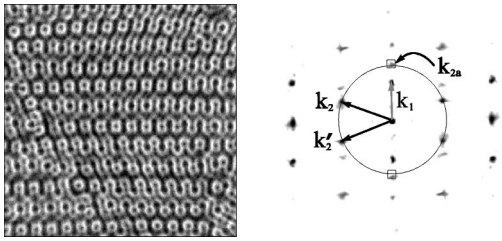

FIG. 41. ''Modulated $2kR$'' states (left) are variants of the $2kR$ states formed when [see the power spectrum (right)] an additional wave vector of magnitude k_2, $\vec{k}_{2b}$, parallel to $\vec{k}_1$ is generated. The system parameters are $\omega_0/(2\pi)=22$ Hz, $\nu=23$ cS, $\phi=0°$, and $h=0.2$ cm.

the subharmonic region of phase space ($\chi>\chi_c$), where square patterns form at threshold. For χ close to χ_c the transition region and the $2kR$ region is relatively narrow compared to the transition region for larger values of χ.

The transition from the square symmetry region to the $2kR$ state is perhaps more interesting than the transition between square and square-2MS states discussed in Sec. VI C. While the square-2MS transition occurs through the formation of an ''additional'' set of wave vectors (of different wave number) that combine with each of the primary wave vectors that initially formed the squares, the square-$2kR$ transition has a qualitatively different nature. Here, the basic square symmetry is not only broken, but is actually *replaced* by a pattern of completely different symmetry. In $2kR$ states, one of the two k_2 wave vectors that are initially perpendicular to each other in the square state is replaced by a k_2 wave vector whose orientation forms the angle θ that is determined by the magnitude of the k_1 wave vector, which defines the $2kR$ rhomboidal pattern.

A typical ''transition'' state at different temporal phases is shown in Fig. 40. The transition occurs through the formation of one or two additional wave vectors of magnitude k_2, $[\vec{k}_{2c}$ in Fig. 40(a)]. These new wave vectors are aligned at the $2kR$ resonant angle θ with respect to the k_2 wave vectors ($\vec{k}_{2a}$ and $\vec{k}_{2b}$) that form the squares. Although additional k_2 vectors could, in theory, form $2kR$ triads with *all* of the original k_2 wave vectors, empirically, we find that only one of the initial k_2 directions is selected. This is possibly due to the fact that the self-interaction of the *harmonic* k_1 wave vectors prefers a hexagonal (rather than a square) arrangement. Thus the transition pattern that is formed is a superposition of a k_2 *square* state with a $2kR$ state. All other wave vectors seen are formed by secondary interactions of these wave vectors. Generally, the transition state breaks the symmetry of the square pattern in a single direction. Since the transition state is usually not global, two domains can form and at their common border, one can observe structures that retain the fourfold symmetry.

In the near vicinity of χ_c, the transition patterns appear as in Fig. 40 and their rhomboidal character is apparent. Farther away from χ_c, the appearance of the transition state is more similar to squares, as the orthogonal k_2 wave vectors are more dominant.

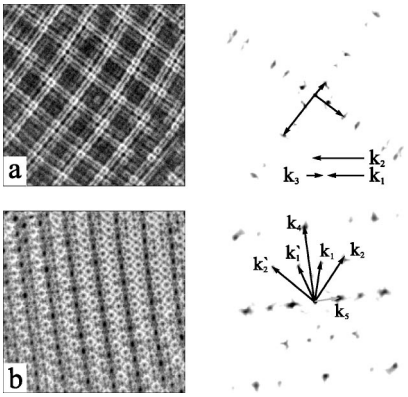

FIG. 42. A $\frac{5}{7}$ ratio yields both the 2MS resonance (a) and a four-wave resonance (b). In the 2MS power spectrum [(a) right] the three vectors are nearly parallel obeying the resonance $\vec{k}_3=\vec{k}_2-\vec{k}_1$. In (b) (right) the power spectrum reveals a qualitatively different resonance: $\vec{k}_1+\vec{k}_1'=\vec{k}_2+\vec{k}_2'\equiv\vec{k}_4$. This resonance produces additional vectors such as $\vec{k}_5$, which are sums and differences of the original wave vectors involved. The experimental parameters are $\frac{55}{77}$ -Hz driving frequencies, $\nu=23$ cS, and $h=0.2$ cm. In (a) $\phi=90°$, $\chi=72.8°$. and in (b) $\phi=0°$, $\chi=70.8°$.

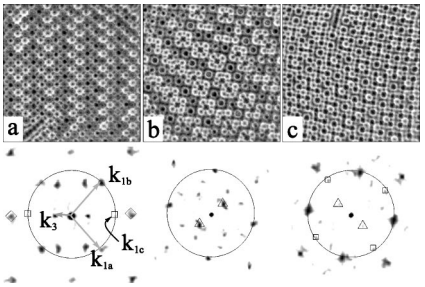

FIG. 43. In an experiment with $\frac{3}{5}$ $\frac{60}{100}$ Hz driving, patterns with square symmetry (or slightly rhombic) dominate for mixing angles $\chi<\chi_c$. The primary wave number is of magnitude k_1 [circles in (a)–(c)]. When the driving is increased, the primary symmetry is broken by a small wave vector of magnitude k_3 (enclosed in triangles). These states are observed for parameters $\nu=23$ cS and $h=0.2$ cm both at mixing angle close to χ_c (a) $\chi=69.6°$ and far from χ_c (b) $\chi=48.1°$ and (c) $\chi=58.7°$. A possible mechanism for the large scale symmetry breaking is a resonant four-wave interaction. The power spectrum [(a), bottom] reveals the existence of additional vectors of magnitude k_1 (enclosed by squares). The interaction of $\vec{k}_{1c}$ with the sum of the original vectors $\vec{k}_{1a}+\vec{k}_{1b}$ (enclosed by diamonds) results in a new vector $\vec{k}_3=\vec{k}_{1c}-(\vec{k}_{1a}+\vec{k}_{1b})$ whose scale is consistent with $k(\omega_0/2)$.

For $\chi>70°$ we observe a variant of the $2kR$ state, shown in Fig. 41, which forms between the ''transition'' and the $2kR$ regions (see Fig. 39). This state, which we call a ''modulated'' $2kR$, consists of a modulation of the regular $2kR$ triad by an additional wave vector of the magnitude and temporal behavior of the larger frequency component. This state is formed by the superposition of a $2kR$ state with an additional wave vector of magnitude k_2 that is oriented parallel to the k_1 wave vector [see Fig. 41 (right)]. This wave vector retains the time dependence of the k_2 mode and generates a spatial and temporal modulation, similar to that induced in the SSS mode, in the $\vec{k}_1$ direction [x in Fig. 31(a)]. A possible mechanism that can generate a ''modulated'' $2kR$ state is a 2MS resonance between the two collinear wave vectors $\vec{k}_1$ and $\vec{k}_2$ that produces a $\vec{k}_3$ wave vector along the same direction. This is verified by comparison with the square-2MS pattern obtained for the same parameters with $\phi=90°$ [see Fig. 34(e)]. This mechanism is supported by our observations of the ''modulated'' $2kR$ states for only relatively low values of ω_0 for which the wave vectors $\vec{k}_1$, $\vec{k}_2$, and $\vec{k}_3$, forming the 2MS state, are nearly parallel.

VIII. ADDITIONAL RESONANT STATES

A. States observed for odd/odd parity driving

The work of Silber, Topaz, and Skeldon [33] indicates that the possible three-wave resonant interactions between excited and damped modes depend on the parity of the driving. For odd/odd driving no three-wave resonant interactions between k_1 and k_2 are expected since both modes are temporally subharmonic (see Sec. I D 1). When considering four-wave interactions, however, these restrictions are no longer valid. Below, we describe two experiments conducted with odd/odd driving, which indeed show that four-wave resonant interactions can be found both in the vicinity of χ_c, where one mode is strongly excited and the other only weakly damped, and far from χ_c where the interactions involve an excited mode and a single strongly damped mode corresponding to the subharmonic frequency $\omega_0/2$.

For $\chi>\chi_c$ a $\frac{5}{7}$ frequency ratio can produce a square-2MS state in the vicinity of χ_c. This, however, is not the only resonantly locked pattern that can be observed at this driving ratio. Mixing angles typically 3°–5° degrees beyond χ_c results in the formation of the state shown in Fig. 42(b). The spatial spectrum of this state indicates that it is formed by a qualitatively different mechanism. The original square pattern, formed by two orthogonal k_2 wave vectors, is broken by an additional pair of k_1 wave vectors, whose orientation is determined by the four-wave resonance condition $\vec{k}_1+\vec{k}_1'=\vec{k}_2+\vec{k}_2'$. This resonance produces additional vectors that are sums and differences of the original wave vectors involved. States similar to these have been previously observed in vertically oscillating convection experiments [61], where three-wave interactions are forbidden.

In odd/odd driving both sides of phase space exhibit subharmonic temporal response. Unlike the $\frac{5}{7}$ driving that produces hexagons for $\chi<\chi_c$ (despite the subharmonic temporal response), experiments performed using $\frac{3}{5}$ driving with $\omega_0=20$ Hz yield square symmetric patterns for $\chi>\chi_c$ and nearly square patterns (rhomboids with an angle of 84°) for $\chi<\chi_c$. Here, a state exhibiting a different mode of four-wave coupling far from χ_c is presented in Fig. 43. Like the SSS states, these patterns result from a symmetry-breaking bifurcation for $\chi_c+20°>\chi>\chi_c$. The power spectrum reveals that in addition to the dominant pair of orthogonal wave vectors ($\vec{k}_{1a}$ and $\vec{k}_{1b}$ in Fig. 43), an additional wave vector of the same magnitude, $\vec{k}_{1c}$, is created along the bi-

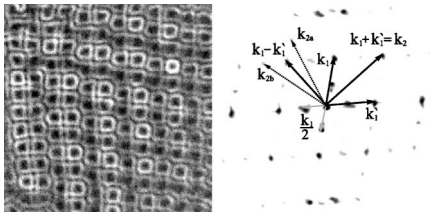

FIG. 44. An image (left) and power spectrum (right) of a spatially subharmonic state where a rhomboid is formed by $\vec{k}_1+\vec{k}_1'=\vec{k}_2$, where k_1 (k_2) is generated by the $5\omega_0$ ($8\omega_0$) frequencies. The pure rhomboid symmetry is broken by two spatially subharmonic vectors $\vec{k}_1/2$ and $\vec{k}_1'/2$. The vectors k_{2a} and k_{2b} are formed by additional resonances: $\vec{k}_{2a}=\vec{k}_1-\vec{k}_1'+\vec{k}_1/2$ and $\vec{k}_{2b}=\vec{k}_1-\vec{k}_1'-\vec{k}_1'/2$. This state appears for $\frac{50}{80}$-Hz driving for $\nu=23$ cS and $h=0.2$ cm for $\chi\sim\chi_c-1°$.

sector of $\vec{k}_{1a}$ and $\vec{k}_{1b}$. The vector sum of these three wave vectors of magnitude k_1 produces a smaller wave vector of magnitude $k_3=\vec{k}_{1c}-(\vec{k}_{1a}+\vec{k}_{1b})$. The scale of $\vec{k}_3$ is consistent with $k(\omega_0/2)$, as determined by the linear dispersion relation. Thus, as in the case of 2MS states, a symmetry-breaking slaved mode $\vec{k}_3$ is excited by a nonlinear resonance.

B. States satisfying more than one resonance condition

We have observed a number of cases where states that satisfy more than a single-resonance condition were selected by the system. These states are generally stable in a relatively wide range of phase space. Here we present a number of examples of such multiply resonant nonlinear states.

We have seen that SSS-I states result from a primary hexagonal symmetry, broken by a wave vector of size $k_c/2$. A similar mechanism can occur for square or rhomboid patterns. In Fig. 44 we show a *spatially* subharmonic state, obtained using $\frac{5}{8}$ driving, where a rhomboid is formed by two wave vectors of magnitude k_1 ($\vec{k}_1$ and $\vec{k}_1'$ in Fig. 44) via the additive $2kR$ resonance $\vec{k}_1+\vec{k}_1'=\vec{k}_2$. The spatial period of the rhomboid is doubled by the appearance of two *new* wave

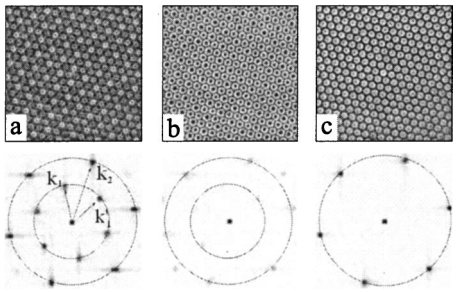

FIG. 45. Images [(a)–(c), top] and the corresponding power spectra [(a)–(c), bottom] of different temporal phases of a SSS-II (2MS) state observed for $\frac{1}{2}$ driving in the harmonic region of phase space at system parameters of $\nu=23$ cS, $\frac{40}{80}$ Hz, and $h=0.155$ cm. The pattern was observed in the vicinity of χ_c for $\chi>\chi_c$. This state resembles SSS-II states observed for $\frac{2}{3}$ driving although here a typical superhexagon cell is $\pi/3$ symmetric whereas the SSS-II state generally has $\pi/6$ rotational symmetry.

FIG. 46. A state formed by simultaneous multiple resonances obtained with $\frac{2}{3}$ driving with the same parameters used to form a $2kR$ state at $\phi=0$, $\omega_0/(2\pi)=20$ Hz, $\nu=23$ cS, $\chi=59°$, and $h=0.2$ cm, but with a phase of $\phi=117°$. The wave vectors of magnitude k_3 are formed both from the resonance $\vec{k}_2-\vec{k}_2'=\vec{k}_3''$ as well as the resonance $\vec{k}_2-\vec{k}_1=\vec{k}_3$. In addition, the condition satisfying the DHS structure is satisfied and the hexagonal sublattice formed by the $\vec{k}_3$ wave vectors spans the entire lattice. k_1, k_2, and k_3 are, respectively, noted by squares, circles, and diamond symbols.

vectors of size $k_1/2$ ($\vec{k}_1/2$ and $\vec{k}_1'/2$ in Fig. 44). This state was observed for a mixing angle $\chi=\chi_c-1°$. An additional spatial resonance is apparent. The vectors $\vec{k}_1-\vec{k}_1'+\vec{k}_1/2$ and $\vec{k}_1-\vec{k}_1'-\vec{k}_1'/2$ both form vectors of length k_2 (see k_{2a} and k_{2b} in Fig. 44). This "extra" four-wave resonance may be the result of spatial mode locking. It may be possible that this extra resonance causes the selection and resultant stability of this state.

Another example of a state satisfying two resonance conditions is presented in Fig. 45. This state, which is only observed in $\frac{1}{2}$ driving experiments, is both a hexagonal 2MS state as well as an SSS-II state. The driving ratio of $\frac{1}{2}$ is unique since ω_3 (given by $\omega_3=\omega_2-\omega_1$) is equal to ω_1. Thus, the wave number k_3, excited by ω_3, coincides with the wave number k_1, excited by ω_1. Therefore [11], a resonant triad is formed involving only the two critical wave numbers k_1 and k_2. In this case SSS-II and 2MS states coincide for $20<\omega_0<50$ Hz. The resonance that is formed is identical to the SSS-II resonance found for odd/even driving in the harmonic region (see Sec. IV B), where the wave vectors of magnitude q and K of the SSS-II state are replaced by wave vectors of respective magnitude k_1 and k_2. The resonance condition for the $\frac{1}{2}$ experiment can be written as $\vec{k}_1+\vec{k}_1'=\vec{k}_2$. The SSS-II-type resonance is possible since, for the system parameters used, the ratio k_2/k_1 is close to $\sqrt{3}$.

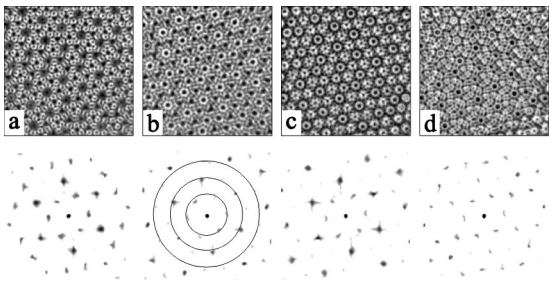

FIG. 47. Different temporal phases of the state described in Fig. 46 taken for constant values of the driving parameters. Circles of radii k_1 (middle circle), k_2 (outer circle), and k_3 (inner circle) are drawn in (b). At different temporal phases, different scales appear dominant.

The same resonance was also observed by Wagner, Muller, and Knorr for a two-mode subharmonic-harmonic interaction in a single-frequency lubrication-limit experiment [41]. In their experiment, for special values of h and ω, two modes with temporal responses of $\omega/2$ and ω and with spatial wave numbers k_1 and k_2 are excited by single-frequency forcing.

In our last example, we present an example of a state where multiple resonance conditions are simultaneously satisfied. When this occurs, we find that the stability of a pattern is significantly enhanced. This state contains features of most of the states described above. This single state includes a 2MS resonance, a DHS resonance (with a $1/\sqrt{7}$ sublattice), an SSS-II-type resonance, and an ''additive'' and ''subtractive'' $2kR$ resonance. This state was observed for $\frac{2}{3}$ driving ($\omega_0=20$ Hz) with $\phi=117°$ and is shown in Fig. 46.

As can be seen in the power spectrum (Fig. 46 right) a double lattice with wave number k_2 at an angle of 22.2° produces the familiar DHS structure described in Sec. III. However, in this case the smallest inner hexagon has a magnitude of k_3, which is associated with frequency, $\omega_3=\omega_2-\omega_1$, while the second inner hexagonal set of wave vectors has a magnitude of k_1. This resonance is very stable and exists in a single domain. This stability is perhaps due its multiply resonant nature. In Fig. 47 a time sequence is shown of the different phases of this state.

IX. CONCLUSIONS

The work described in this paper provides a partial, but coherent, experimental picture of both the nonlinear states generated by two-frequency forcing as well as their domains of existence in phase space, and the nonlinear interactions that generate them. As demonstrated above, the space of nonlinear patterns formed by two interacting unstable modes is very rich. Our understanding of the types of structures and their selection is just beginning. Predicted nonlinear three-wave resonances [30], however, appear to govern nonlinear pattern selection only for the *simplest* ratios ($\frac{2}{3}$ and $\frac{1}{2}$). Recent theoretical advances made by Silber and co-workers in the analysis of the two-frequency Faraday system in the vicinity of the codimension-2 point [30,33] suggest that at least some of the features discovered by our experiments can be reproduced by amplitude equations derived using the quasipotential approximation (e.g., [11]). In addition, recent work [23,34,40] indicates that many of the superlattice states found far from χ_c may be qualitatively understood as representations of invariant subgroups of broken hexagonal symmetry. A quantitative theory that describes the important regime of two or more concurrently unstable modes for arbitrary height and viscosity has still to be developed.

Some of the major results of this work are summarized below.

(1) The temporal symmetry of the driving determines which resonant interactions *can* occur between the primary excited modes. A number of distinct three- and four-wave interactions between excited modes and between slaved and excited modes were experimentally observed.

(2) Factors such as the dimensionless dissipation in the system and the driving phase ϕ can play an important role in the nonlinear interaction mechanism selected by the system. ϕ is a convenient parameter for comparison with theory, as, in contrast to the system's dissipation, its value does not play a role in the validity of the theoretical (e.g., [11]) approximation used.

(3) Symmetry breaking can often occur via modes that nonlinearly couple to the original set of modes. The symmetry-breaking modes tend to be arranged in invariant subgroups of the original symmetry group.

(4) In many cases, linearly stable slaved modes can be nonlinearly excited by the parametrically amplified nonlinear modes. The number and availability of slaved modes (determined by the ratio of the driving frequencies) is important in the selection of the final nonlinear states. This provides a nontrivial selection mechanism for nonlinear states.

(5) A theoretically predicted mechanism [25,26] for producing quasipatterns was experimentally observed. By tuning the system parameters to satisfy a resonance condition $2n$-fold quasipatterns can be produced for any desired n.

We believe that both the states and nonlinear mechanisms described in this work should be of general importance to a wide class of parametrically driven nonlinear systems. Such systems include parametrically driven fluid systems, nonlinear optical systems [43,50,62–64], nonlinear wave interactions in superfluid helium [65,66], magnetically driven ferrofluids [44], and possibly nonlinearly coupled mechanical systems. The behavior of systems driven by two-frequency forcing is, itself, important. Understanding the spatiotemporal behavior of such systems is but a first step in understanding the general behavior in space and time of nonlinear systems driven by multiple frequencies. The work presented here is an important building block on the road to understanding these more complex systems.

ACKNOWLEDGEMENT

We gratefully acknowledge the support of the Israel Academy of Sciences (Grant No. 203/99).

[1] S. Douady, J. Fluid Mech. **221**, 383 (1990).
[2] D. Binks and W. van de Water, Phys. Rev. Lett. **78**, 4043 (1997).
[3] A. Kudrolli and J. P. Gollub, Physica D **97**, 133 (1996).
[4] K. Kumar and K. M. S. Bajaj, Phys. Rev. E **52**, R4606 (1995).
[5] E. Bosch and W. van de Water, Phys. Rev. Lett. **70**, 3420 (1993).
[6] S. Ciliberto, S. Douady, and S. Fauve, Europhys. Lett. **15**, 23 (1991).
[7] A. B. Ezerskii, M. I. Rabinovich, V. P. Reutov, and I. M. Starobinets, Zh. Eksp. Teor. Fiz. **91**, 2070 (1986) [Sov. Phys. JETP **64**, 1228 (1986)].
[8] B. J. Gluckman, P. Marcq, J. Bridger, and J. P. Gollub, Phys. Rev. Lett. **71**, 2034 (1993).

[9] A. Kudrolli and J. P. Gollub, Phys. Rev. E **54**, R1052 (1996).
[10] L. Daudet, V. Ego, S. Manneville, and J. Bechhoefer, Europhys. Lett. **32**, 313 (1995).
[11] W. Zhang and J. Vinals, J. Fluid Mech. **341**, 225 (1997).
[12] H. W. Muller, Phys. Rev. Lett. **71**, 3287 (1993).
[13] T. Besson, W. S. Edwards, and L. S. Tuckerman, Phys. Rev. E **54**, 507 (1996).
[14] K. Kumar, Proc. R. Soc. London, Ser. A **452**, 1113 (1996).
[15] H. Arbell and J. Fineberg, Phys. Rev. Lett. **81**, 4384 (1998).
[16] W. S. Edwards and S. Fauve, C. R. Acad. Sci., Ser. II: Mec., Phys., Chim., Sci. Terre Univers **315**, 417 (1992).
[17] W. S. Edwards and S. Fauve, Phys. Rev. E **47**, R788 (1993).
[18] W. S. Edwards and S. Fauve, J. Fluid Mech. **278**, 123 (1994).
[19] H. Arbell and J. Fineberg, Phys. Rev. Lett. **85**, 756 (2000).
[20] P. B. Umbanhowar, F. Melo, and H. L. Swinney, Nature (London) **382**, 793 (1996).
[21] A. Kudrolli, B. Pier, and J. P. Gollub, Physica D **123**, 99 (1998).
[22] H. Arbell and J. Fineberg, Phys. Rev. Lett. **84**, 654 (2000).
[23] M. Silber and M. R. E. Proctor, Phys. Rev. Lett. **81**, 2450 (1998).
[24] D. Binks, M. T. Westra, and W. van de Water, Phys. Rev. Lett. **79**, 5010 (1997).
[25] H. W. Muller, Phys. Rev. E **49**, 1273 (1994).
[26] T. Frisch and G. Sonnino, Phys. Rev. E **51**, 1169 (1995).
[27] R. Lifshitz and D. M. Petrich, Phys. Rev. Lett. **79**, 1261 (1997).
[28] A. C. Newell and Y. Pomeau, J. Phys. A **26**, L429 (1993).
[29] W. Zhang and J. Vinals, J. Fluid Mech. **336**, 301 (1997).
[30] M. Silber and A. C. Skeldon, Phys. Rev. E **59**, 5446 (1999).
[31] J. D. Crawford, Rev. Mod. Phys. **63**, 991 (1991).
[32] J. D. Crawford, Physica D **52**, 429 (1991).
[33] M. Silber, C. M. Topaz, and A. C. Skeldon, Physica D **143**, 205 (2000).
[34] D. P. Tse, A. M. Rucklidge, R. B. Hoyle, and M. Silber, Physica D **146**, 367 (2000).
[35] K. Kumar and L. S. Tuckerman, J. Fluid Mech. **279**, 49 (1994).
[36] O. Lioubashevski, J. Fineberg, and L. S. Tuckerman, Phys. Rev. E **55**, R3832 (1997).
[37] F. Simonelli and J. P. Gollub, J. Fluid Mech. **199**, 471 (1989).
[38] O. Lioubashevski *et al.*, Phys. Rev. Lett. **83**, 3190 (1999).
[39] O. Lioubashevski, H. Arbell, and J. Fineberg, Phys. Rev. Lett. **76**, 3959 (1996).
[40] A. M. Rucklidge, M. Silber, and J. Fineberg, in *Bifurcations, Symmetry and Patterns*, edited by J. Buescu *et al.* (Birkhäuser, Basel, in press).
[41] C. Wagner, H. W. Muller, and K. Knorr, Phys. Rev. E **62**, R33 (2000).
[42] C. Wagner, H. W. Muller, and K. Knorr, Phys. Rev. Lett. **83**, 308 (1999).
[43] A. Logvin, Y. T. Ackemann, and W. Lange, Phys. Rev. A **55**, 4538 (1997).
[44] H. J. Pi, S. Y. Park, J. Lee, and K. J. Lee, Phys. Rev. Lett. **84**, 5316 (2000).
[45] T. Ackemann, Y. A. Logvin, A. Heuer, and W. Lange, Phys. Rev. Lett. **75**, 3450 (1995).
[46] R. Herrero *et al.*, Phys. Rev. Lett. **82**, 4627 (1999).
[47] J. L. Hammack and D. M. Henderson, Annu. Rev. Fluid Mech. **25**, 55 (1993).
[48] E. Pampaloni, S. Residori, S. Soria, and F. T. Arecchi, Phys. Rev. Lett. **78**, 1042 (1997).
[49] J. Fineberg and V. Steinberg, Phys. Rev. Lett. **58**, 1332 (1987).
[50] A. V. Mamaev and M. Saffman, Phys. Rev. Lett. **80**, 3499 (1998).
[51] W. Zimmermann *et al.*, Europhys. Lett. **24**, 217 (1993).
[52] A. J. Scroggie and W. J. Firth, Phys. Rev. A **53**, 2752 (1996).
[53] M. Hoyuelos, P. Colet, M. S. Miguel, and D. Walgraef, Phys. Rev. E **58**, 2992 (1998).
[54] M. Bachir, S. Metens, P. Borckmans, and G. Dewel, Europhys. Lett. **54**, 612 (2001).
[55] E. A. Kuznetsov, A. A. Nepomnyashchy, and L. M. Pismen, Phys. Lett. A **205**, 261 (1995).
[56] G. H. Gunaratne, Q. Ouyong, and H. L. Swinney, Phys. Rev. E **50**, 2802 (1994).
[57] P. C. Matthews, Physica D **116**, 81 (1998).
[58] P. Hall and R. E. Kelly, Phys. Rev. E **52**, 3687 (1995).
[59] M. Yethiraj, D. M. Paul, C. V. Tomy, and E. M. Forgan, Phys. Rev. Lett. **78**, 4849 (1997).
[60] U. Breiner, U. Krappe, E. L. Thomas, and R. Stadler, Macromolecules **31**, 135 (1998).
[61] J. L. Rogers, M. F. Schatz, O. Brausch, and W. Pesch, Phys. Rev. Lett. **85**, 4281 (2000).
[62] M. Tlidi, P. Mandel, and M. Haelterman, Phys. Rev. E **56**, 6524 (1997).
[63] R. Martin, A. J. Scroggie, G. L. Oppo, and W. J. Firth, Phys. Rev. Lett. **77**, 4007 (1996).
[64] D. Leduc, M. LeBerre, E. Ressayre, and A. Tailet, Phys. Rev. A **53**, 1072 (1996).
[65] D. Rinberg, V. Cherepanov, and V. Steinberg, Phys. Rev. Lett. **76**, 2105 (1996).
[66] D. Rinberg, V. Cherepanov, and V. Steinberg, Phys. Rev. Lett. **78**, 4383 (1997).